BBA - Molecular Basis of Disease 1871 (2025) 167556

Contents lists available at ScienceDirect

BBA - Molecular Basis of Disease

journal homepage: www.elsevier.com/locate/bbadis

Mitochondrial respiratory complex II is altered in renal carcinoma

Sona Miklovicova [a,b], Luca Volpini [a,c], Ondrej Sanovec [a,b], Federica Monaco [c], Katerina Hadrava Vanova [d], Jaromir Novak [a,b], Stepana Boukalova [a], Renata Zobalova [a], Petr Klezl [e], Marco Tomasetti [c], Vladimir Bobek [e,f,g], Vojtech Fiala [h], Josef Vcelak [i], Lory Santarelli [c], Zuzana Bielcikova [h], Katerina Komrskova [a,b], Katarina Kolostova [e], Karel Pacak [d], Sarka Dvorakova [a,*], Jiri Neuzil [a,b,j,k,**]

[a] *Institute of Biotechnology, Czech Academy of Sciences, 252 50 Prague-West, Czech Republic*
[b] *Faculty of Science, Charles University, 128 00 Prague, Czech Republic*
[c] *Department of Clinical and Molecular Sciences, Polytechnic University of Marche, 60126 Ancona, Italy*
[d] *Eunice Kennedy Shriver National Institute of Child Health and Human Development, National Institutes of Health, Bethesda, MD 20892, USA*
[e] *General University Hospital Kralovske Vinohrady, 100 34 Prague, Czech Republic*
[f] *Department of Thoracic Surgery, Krajska zdravotni a.s. and UJEP, 400 11 Usti and Labem, Czech Republic*
[g] *Department of Thoracic Surgery, Faculty of Medicine, Wroclaw University of Science and Technology, 51 377 Wroclaw, Poland*
[h] *General University Hospital, 128 08 Prague, Czech Republic*
[i] *Department of Molecular Endocrinology, Institute of Endocrinology, 110 00 Prague, Czech Republic*
[j] *School of Pharmacy and Medical Science, Griffith University, Southport, Qld 4222, Australia*
[k] *First Faculty of Medicine, Charles University, 121 08 Prague, Czech Republic*

ARTICLE INFO

Keywords:
Complex II
Succinate dehydrogenase
Renal cell carcinoma
Metabolism
Mitochondria
Organoids

ABSTRACT

Background: Renal cell carcinoma (RCC) is a disease typified by anomalies in cell metabolism. The function of mitochondria, including subunits of mitochondrial respiratory complex II (CII), in particular SDHB, are often affected. Here we investigated the state and function of CII in RCC patients.

Methods: We evaluated tumour tissue as well as the adjacent healthy kidney tissue of 78 patients with RCC of different histotypes, focusing on their mitochondrial function. As clear cell RCC (ccRCC) is by far the most frequent histotype of RCC, we focused on these patients, which were grouped based on the pathological WHO/ISUP grading system to low- and high-grade patients, indicative of prognosis. We also evaluated mitochondrial function in organoids derived from tumour tissue of 7 patients.

Results: ccRCC tumours were characterized by mutated von Hippel-Lindau gene and high expression of carbonic anhydrase IX. We found low levels of mitochondrial DNA, protein and function, together with CII function in ccRCC tumour tissue, but not in other RCC types and non-tumour tissues. Mitochondrial content increased in high-grade tumours, while the function of CII remained low. Tumour organoids from ccRCC patients recapitulated molecular characteristics of RCC tissue.

Conclusions: Our findings suggest that the state of CII, epitomized by its assembly and SDHB levels, deteriorates with the progressive severity of ccRCC. These observations hold the potential for stratification of patients with worse prognosis and may guide the exploration of targeted therapeutic interventions.

1. Introduction

Renal cell carcinoma (RCC) is a hard-to-manage pathology. In spite of significant progress over the last decades in the diagnosis and treatment of RCC, patient outcome and prognosis remain poor [1,2]. This includes diverse histological subtypes such as clear cell, papillary, and chromophobe types of RCC. These subtypes vary in their cellular origins, with the clear cell (ccRCC) and papillary types arising from cells of the proximal convoluted tubule, while the chromophobe type originates from cells of the distal convoluted tubule within the nephron [3].

---

[*] Corresponding author.
[**] Correspondence to: J. Neuzil, Institute of BIotechnology, Czech Academy of Sciences, 252 50, Prague-West, Czech Republic.
E-mail addresses: sarka.dvorakova@ibt.cas.cz (S. Dvorakova), j.neuzil@griffith.edu.au, jiri.neuzil@ibt.cas.cz (J. Neuzil).

https://doi.org/10.1016/j.bbadis.2024.167556
Received 10 April 2024; Received in revised form 18 October 2024; Accepted 28 October 2024

The most frequent ccRCC stands out among various malignancies due to its intricate metabolic reprogramming, primarily orchestrated by Von Hippel-Lindau (*VHL*) gene pathogenic variations [4] and the consequent modulation of hypoxia-inducible factors (HIFs), leading to upregulation of hypoxia-responsive genes [5]. These underlying alterations fuel tumour development, progression and metastasis, highlighting the urgency to dissect mitochondrial perturbations. From a clinical standpoint, ccRCC shows resistance to traditional cytotoxic drugs, with treatment strategies typically involving surgical interventions and targeted therapies like tyrosine kinase inhibitors, mTOR inhibitors, and immunotherapy [6]. Linked to this is the notion that high-grade (G3/4) patients exhibit markedly worse prognosis compared to low-grade (G1/2) patients [7]. Hence, it is of paramount importance to search for novel biomarkers and for improved targeted therapies.

Of particular interest in the case of ccRCC is the complex interplay between mitochondrial respiratory complex II (CII; succinate dehydrogenase, SDH) and the tumorigenic process. Although CII mutations are relatively rare in RCC [8], altered CII status has emerged as a notable negative prognostic marker in ccRCC [9], warranting a comprehensive investigation of RCC mitochondrial properties with focus on CII status and its assembly dynamics [10]. CII is at the crossroads of the Krebs cycle and oxidative phosphorylation (OXPHOS) as SDH, by means of its enzymatic activity, converts succinate to fumarate within the Krebs cycle, and the resulting electrons enter the electron transport chain (ETC), a step catalyzed by the succinate:quinone reductase (SQR) activity of CII [11]. CII is located at the inner mitochondrial membrane (IMM) and is composed of four nuclear-encoded subunits (SDHA, SDHB, SDHC, and SDHD). SDHA and SDHB are hydrophilic and are localized in the matrix, while SDHC and SDHD are hydrophobic and are buried in the IMM. Assembly of these subunits into CII is crucial for its function [10,11].

CII assembly is a complex process that involves maturation of its catalytic subunit SDHA as its crucial milestone, as we have recently reported [12]. We demonstrated that maturation of SDHA is step-wise, involving disordered-to-ordered alterations and sequential binding of assembly factors SDHAF2 and SDHAF4. Disruption of CII subunits or assembly factors leads to CII collapse or its aberrant assembly, resulting in metastable sub-assemblies referred to as CII_{low}, comprising SDHA alone or together with the assembly factors SDHAF2 and/or SDHAF4. Presence of CII_{low} indicates a stress situation [13].

We have recently conducted a Phase 1/1b clinical trial of MitoTam, an agent targeting mitochondrial complex I [14], where we found high benefit for ccRCC patients [15,16]. This is highly promising and indicates that MitoTam may be able to be developed into an efficient drug against RCC. It was recently proposed that anomalies in CII affect the level and assembly of CI, the target of MitoTam [17]. We therefore decided to systematically explore tumour tissue and the corresponding healthy kidney tissue for the state of CII.

2. Material and methods

2.1. Patients and tissue specimens

Tissue samples were obtained from patients undergoing total nephrectomy in 2 centers, i.e. University Hospital Kralovske Vinohrady (49 cases) and General University Hospital (29 cases), Prague, Czech Republic, between 2021 and 2024; and were inspected and reviewed by skilled pathologists. Tumours were graded according to the WHO/ISUP (World Health Organization/International Society of Urological Pathology) classification. Details of patients are presented in Table 1. Samples were transported to the laboratory on ice in the RPMI-1640 medium supplemented with 10 % fetal bovine serum (FBS) and 1 % penicillin/streptomycin (P/S) for immediate processing and stored at −80 °C till further analysis. In certain cases, the samples were analysed immediately, prior to freezing. Due to different requirements for fresh tissue and different amount of available patient material, individual assays were performed on different number of patient samples.

Table 1
Patient characteristics.

Parameter	Number of patients	%
(years) Age at diagnosis		
30–39	4	5
40–49	7	9
50–59	19	24
60–69	20	26
70–79	24	31
80–89	4	5
Gender		
Female	27	35
Male	51	65
Histology		
Clear cell	64	82
Papillary	8	10
Chromophobe	5	7
Oncocytoma	1	1
Grade		
Low (G1/2)	53	68
High (G3/4)	18	23
N/A	7	9
(cm) Tumour diameter		
1–2.9	10	13
3–5.9	34	44
6–8.9	18	23
9–12	8	10
N/A	8	10
TNM		
Benign	1	1
T1	33	45
T1N1	1	
T1M1	1	
T2	4	5
T3	33	49
T3N1	1	
T3M1	4	
Total	78	100

Ethics approval and consent to participate in the study was performed in accordance with the Declaration of Helsinki and was approved by the Ethical Review Committee of the Czech Health Research Agency, Reference number EK-VP/23/0/2022 and EK-VP/47/0/2020.

2.2. Primary cell culture

All chemicals were purchased from Sigma-Aldrich unless otherwise stated in the text. Tumour tissue samples were washed in cold PBS, minced and incubated for 1 h at 37 °C with DMEM/F12 medium (Lonza) supplemented with 1 % P/S, 5 mg/ml collagenase type II (Gibco) and 10 μM Y-27632. After enzymatic digestion, tissues were centrifuged at 200 *g* for 5 min at room temperature (RT). The supernatant was then discarded, and the pellet was incubated for 3 min at 37 °C with TrypLE Express Enzyme (Gibco). Trypsinization was neutralized with 20 % FBS and samples were centrifuged at 200 *g* for 5 min. The supernatant was then discarded and dissociated cell pellets were filtered through 100 μm cell strainers after resuspension in DMEM/F12 supplemented with 20 % FBS and 10 μM Y-27632. Dissociated and filtered cells were centrifuged at 200 *g* for 5 min, resuspended in organoid culture medium: DMEM/F12 supplemented with 10 % FBS, 1 % P/S, 10 ng/ml human epidermal growth factor (EGF), 5 μg/ml insulin and 0.4 μg/ml hydrocortisone; and seeded into T25 flasks. When confluent, primary cell cultures were frozen at −80 °C in a solution of FBS with 10 % DMSO to establish patient-derived organoids.

2.3. Patient-derived organoid formation

Cell suspension corresponding to 70–80 % cell confluence was centrifuged at 200 *g* for 5 min at RT and resuspended in the same volume of ice-cold Matrigel (Corning). Drops of 20–25 μl of Matrigel-embedded cells were seeded into a 24-well plate and after solidification in the CO_2 incubator at 37 °C, 1 ml of the organoid culture medium was added to each well. Organoids were cultured for 2 weeks with medium changed every 3 days.

2.4. Histology and immunohistochemistry

After fixation in 4 % formaldehyde, organoids were embedded in 3 % agarose/PBS, followed by dehydration, paraffin embedding, sectioning, and standard hematoxylin and eosin (H&E) staining. Immunohistochemistry (IHC) staining was performed on paraffin sections (2 μm). Briefly, after deparaffinization and rehydration, sections underwent heat-mediated antigen retrieval. Endogenous peroxidase activity was neutralized by 20 min incubation with 3 % H_2O_2/methanol, followed by 1 h antigen blocking with 2 % bovine serum albumin (BSA). Sections were incubated with anti-carbonic anhydrase IX (CAIX) primary antibody (1:1000; Novus Biologicals, NB100–417). The primary antibody was diluted in the antibody diluent (Zytomed Systems) and incubated for 2 h at RT. Sections were subsequently incubated with ZytoChem Plus (HRP) One-Step Polymer anti-mouse/rabbit (Zytomed Systems) and visualized using a Liquid DAB+ substrate Chromogen System (Dako). Nuclei were counterstained with hematoxylin, and coverslips were mounted with the DPX (dibutylphthalate, polystyrene, xylene) reagent. Images were acquired using an optical microscope (DMi8 WF, Leica; 40× magnification).

2.5. Immunofluorescence

Immunofluorescence (IF) staining was performed on paraffin sections (2 μm). Briefly, after deparaffinization and rehydration, sections underwent heat-mediated antigen retrieval. After washing in PBS, sections were permeabilized with 0,05 % Tween20/PBS and incubated 1 h antigen blocking with 2 % bovine serum albumin (BSA). Subsequently, sections were incubated with anti-CAIX and anti-MT-CO1 primary antibodies (CAIX, 1:500, Novus Biologicals, NB100–417; MT-CO1, 1:100, Abcam, ab14705). The primary antibody was diluted in the antibody diluent (Zytomed Systems) and incubated for 2 h at RT. After additional washes in 0.05 % Tween20/PBS, sections were labelled with respective secondary antibodies (goat-anti-mouse AlexaFluorPlus 488, 1:300, Invitrogen, A32723 and goat-anti-rabbit AlexaFluorPlus 594, 1:300, Invitrogen, A32740). Final steps included further washes in 0.05 % Tween20/PBS and dH_2O followed by mounting with Vectashield containing DAPI (VECTASHIELD® Antifade Mounting Medium with DAPI Vector Laboratories H-1200-10). Sections were imaged using Nikon CSU-W1 confocal microscope, 20× CFI Plan Apo VC (NA = 0.75) objective and PRIME BSI camera (Teledyne Photometrics, 6.5 μm pixel size). using 405, 488 and 594 lasers complemented with corresponding emission filters (455/50, 525/50, 645/75). The unbiased quantification of mitochondria (MT-CO1) signal on healthy and tumour tissues was performed using FIJI software. To compare MT-CO1 level between healthy and tumour tissues, the nuclear (DAPI) signal was utilized to delineate tissue areas. This process involved denoising, background subtraction, and contrast enhancement, followed by automated local thresholding using the Bernsen method to create a mask. The same procedure was applied to compare MT-CO1 levels between tumour tissues and tumour organoids, with normalization to the CAIX membrane signal. The mean intensity of the MT-CO1 signal within the delineated tissue areas was measured using ImageJ.

2.6. CLARITY imaging

Organoids were processed using the CLARITY procedure [18]. Briefly, organoids were fixed in the CLARITY gel monomer containing 4 % formaldehyde for 2 h. After gel polymerization, organoids were cleared overnight in the clearing buffer (20 mM lithium hydroxide monohydrate and 200 mM SDS, pH 8,5) at 37 °C with gentle shaking. The next day, organoids were stained with DAPI and the lipophilic FM™ 4-64FX dye (Invitrogen). Stained organoids were mounted in the PROTOS refractive index matching solution. *Z*-stack images were acquired using the Carl Zeiss LSM 880 NLO confocal microscope (LD LCI Plan-Apochromat420852–9871, magnification 25× N.A. 0.8). For 3D visualization and surface rendering, the Imaris software, v. 9.8.2 Package for Cell Biologists was used.

2.7. DNA and RNA isolation

Fresh-frozen tissues and cultured organoids were homogenized using 5 mm Stainless Steel Beads (Qiagen) and the Qiagen TissueLyser LT (Qiagen). DNA and RNA were extracted using the AllPrep DNA/RNA/Protein Mini Kit (Qiagen) for tissues and AllPrep DNA/RNA/Protein Micro Kit (Qiagen) for organoids according to the manufacturer's instructions. The concentration and purity of isolated DNA and RNA were assessed using a spectrophotometer (Nanodrop 2000 Instrument, Thermo Fisher Scientific), and the samples were stored at −80 °C until further analysis.

2.8. Genomic analysis of *VHL* gene using next generation sequencing

Genomic analysis was performed to characterize genetic alterations of the *VHL* gene using next-generation sequencing (NGS). Extracted DNA was amplified to generate 566 bp, 376 bp and 433 bp sequences of *VHL* exons 1, 2 and 3 using polymerase chain reaction (PCR) with primer pairs for exon 1: 5’-CGC GAA GAC TAC GGA GGT-3′ and 5′-GGA TGT GTC CTG CCT CAA G-3′, for exon 2: 5’-ACC GGT GTG GCT CTT TAA CA-3′ and 5’-GCC CAA AGT GCT TTT GAG AC-3′ and for exon 3: 5′-TGG CAA AGC CTC TTG TTC G-3′ and 5’-GCC CCT AAA CAT CAC AAT GCC-3′. 100 ng DNA was amplified with 1 μM of each primer and 1× Dream Taq PCR Master Mix (Thermo Fisher Scientific) in the final volume of 20 μl. 4 % DMSO was added to PCR reaction for exon 1. Cycling conditions were: denaturation step at 95 °C for 2 min followed by 35 cycles of denaturation at 95 °C for 20 s, annealing at 60 °C for 30 s (exons 2 and 3), or annealing at 53 °C for 30 s (exon 1), primer extension at 72 °C for 2 min and one final run-off extension at 72 °C for 10 min. All PCR products were visualized by electrophoresis using 2 % agarose gel in the TAE buffer. Libraries were prepared from purified PCR products of the *VHL* gene (exons 1, 2 and 3) using the Nextera XT DNA Library Prep Kit (Illumina) according to the manufacturer's sample preparation protocol and subsequently paired-end sequenced for 300 cycles by the MiSeq Reagent Kit v.2 on a MiSeq sequencer platform (Illumina). Sequence data were analysed by the on-instrument software Local Run Manager v.4 with DNA Amplicon Analysis Module v.2.1.0 (Illumina) with the option for somatic variant calling method from the Variant Caller. The data were demultiplexed and FASTQ files were generated. Reads from paired-end fragments were trimmed for low-quality and duplicate reads. The Local Run Manager software aligned the reads against the human reference sequence GRCH37.p5/hg19 using the Burrows-Wheeler Aligner (BWA) and Genome Analysis Toolkit (GATK, Broad Institute). All variants were visualized with the Integrative Genomics Viewer (UC San Diego, Broad Institute). The detected single-nucleotide variants and small insertions/deletions were annotated and filtered for exonic non-synonymous variants, variants with a probable splice site or frameshift effect and prediction of functional pathogenic effects in genetic databases ClinVar (http://www.ncbi.nlm.nih.gov/clinvar/) and VarSome (www.varsome.com).

2.9. Real-time PCR

1 μg RNA was reverse-transcribed into cDNA with random hexamer primers using Revert Aid First strand cDNA Synthesis Kit (Thermo Scientific). Target genes were amplified by real-time and fluorescent polymerase chain reaction using the 5xHOT FirePol Evagreen qPCR Supermix (Solis Biodyne) and the CFX96 Touch Real-Time PCR Detection System (BioRad). Relative mRNA levels were calculated as the fold change using the 2 — ΔΔCT formula and were normalized to *GAPDH*. Primers were designed as follows: *SDHA* forward (5′- GAG ATG TGG TGT CTC GGT CCA T-3′), *SDHA* reverse (5′-GCT GTC TCT GAA ATG CCA GGC A-3′); *SDHB* forward (5′-CAG TCC ATA GAA GAG CGT GAG-3′), *SDHB* reverse (5′-TGT CTC CGT TCC ACC AGT AGC T-3′); *SDHAF2* forward (5′-CCA TAG AAA CCA AAA GAG CCC GC-3′), *SDHAF2* reverse (5′-AGG CGG TCA TAG AGG TTC AGC T-3′); *GAPDH* forward (5′- GTC GGA GTC AAC GGA TTT GG -3′), *GAPDH* reverse (5′- AAA AGC AGC CCT GGT GAC C-3′). The ratio of mitochondrial to nuclear DNA (mtDNA:nDNA) was analysed using primers for major arc of mtDNA: *MajArc* forward (5'-CTG TTC CCC AAC CTT TTC CT-3′), *MajArc* reverse (5'-CCA TGA TTG TGA GGG GTA GG-3′); and nuclear DNA primers for β2-microglobulin: ***β2M*** forward (5'-GCT GGG TAG CTC TAA ACA ATG TAT TCA-3′), ***β2M*** reverse (5'-CCA TGT ACT AAC AAA TGT CTA AAA TGG T-3′). Cycling conditions were: denaturation step at 95 °C for 2 min followed by 39 cycles of denaturation at 95 °C for 15 s, annealing at 60 °C for 20 s, and primer extension at 72 °C for 20 s.

2.10. High-resolution respirometry

6 mg of fresh healthy kidney and 14.5 mg of fresh tumour tissue were homogenized in the total volume of 2 ml of Mir05 medium (0.5 mM EGTA, 3 mM $MgCl_2$, 60 mM K-lactobionate, 20 mM taurine, 10 mM KH_2PO_4, 110 mM sucrose, 1 g/l essentially fatty acid-free BSA, and 20 mM HEPES, pH 7.1) using the PBI-Shredder O2k-Set (Oroboros), and transferred to the 2-ml chamber of the Oxygraph 2 k instrument (Oroboros). CII-mediated respiration was determined in the presence of 0.5 μM rotenone, 10 mM succinate, 3 mM ADP, and 10 μM cytochrome *c* at 37 °C. CII-specific oxygen-consumption rates were verified by the addition of 5 mM malonate. Antimycin A (2.5 μM) was added at the end of each assay to inhibit the electron transport chain, and residual oxygen consumption after antimycin A addition was subtracted from all results in order to obtain mitochondria-specific rates. Next, CIV activity was assessed after addition of 2 mM ascorbate and 0.5 mM tetramethyl-*p*-phenylenediamine (TMPD), followed by its inhibition with 1.25 mM potassium cyanide (KCN).

2.11. Citrate synthase activity

Citrate synthase (CS) activity was assessed spectrophotometrically using 10 μl tissue extracts after respirometry assays. Enzyme activity was determined by adding 0.31 mM acetyl-CoA, 0.5 mM oxalacetate and 0.1 mM 5,5′-dithiobis(2-nitrobenzoic acid) (DTNB). The absorbance at 412 nm was recorded for 30 min at 30 °C to measure the reaction product thionitrobenzoic acid (TNB) using a microplate reader (Infinite M200, Tecan). Regression analysis of the linear portion of the curve was performed using GraphPad PRISM software (v.8.4.3).

2.12. SDS-PAGE/western blotting

Tissues and organoids were homogenized in the Radio-ImmunoPrecipitation Assay (RIPA) buffer containing 20 mM Tris (pH 7.5), 150 mM NaCl, 1 mM EDTA, 1 mM EGTA, 1 % (*v*/v) NP-40, 0.1 % SDS and 0.5 % sodium deoxycholate supplemented with the protease inhibitor mix M (Serva) buffer using 5 mm Stainless Steel Beads (Qiagen) and TissueLyser LT (Qiagen). The solution was shaken for 1 h on ice. Lysed tissue was centrifuged at 16,000 *g* for 5 min at 4 °C, and the supernatant was collected for analysis. Total protein was quantified by the Pierce BCA Protein Assay Kit (Thermo Scientific). Following boiling in the 4×Laemmli sample loading buffer (8 % SDS, 260 mM Tris-HCl, pH 6.8, 40 % glycerol, 200 mM DTT, 0.01 % bromophenol blue) for 5 min, 40 μg of the denatured protein was loaded and separated using 12 % SDS-PAGE gel. Wet blotting was used to transfer the separated proteins to 0.45 μm pore nitrocellulose membrane (BioRad). The membrane was blocked with 5 % non-fat milk for 1 h and incubated overnight at 4 °C with the diluted solutions (1:1,000) of primary antibodies in Tris-buffered saline/Tween-20 (TBS-T) supplemented with 2 % non-fat milk. The following primary antibodies were used: anti-Hsp60 (12,165, Cell Signaling), anti-β-actin (8457S, Cell Signaling), anti-SDHA (ab14715, Abcam), anti-SDHB (ab14714, Abcam), anti-SDHAF2 (45,849, Cell Signaling), anti-CAIX (NB100–417, Novus), anti-Tomm20 (sc11415, Santa Cruz). Horseradish peroxidase-conjugated secondary antibodies were used in TBS-T with 2 % non-fat dried milk for 1 h at RT (1:5000 for goat anti-mouse IgG (170–6516, BioRad); and goat anti-rabbit IgG (170–6515, Biorad)). Protein bands were detected by the chemiluminescent HRP substrate (Radiance ECL or Radiance Plus, Azure Biosystems) using the Azure 600 Instrument and AzureSpot 2.0 Software (Azure Biosystems). The intensity of each band was evaluated by ImageJ software (ImageJ, v.1.8.0), and was normalized according to the β-actin level.

2.13. Isolation of mitochondria

To isolate mitochondria, healthy kidney and tumour tissues were homogenized on ice in the isolation buffer (225 mM mannitol, 75 mM sucrose, 5 mM HEPES-KOH, pH 7.4, 1 mM EGTA) with 1 % BSA using chilled Dounce Tissue Grinder (Kimble Chase, DWK Life Sciences). The homogenate was centrifuged at 1000 *g* for 10 min at 4 °C. The supernatant containing mitochondria was collected and then centrifuged at 10,000 *g* for 10 min to pellet mitochondria. Pelleted mitochondria were washed with the isolation buffer and stored at —80 °C.

2.14. Native blue gel electrophoresis/western blotting

10 μg digitonin-solubilized (8 g/g protein) mitochondria were mixed with the sample loading buffer (0.015 μl per 1 μg protein; 0.75 M aminocaproic acid, 50 mM Bis-Tris, 12 % glycerol, 0.5 mM EDTA, 5 % Coomassie Brilliant Blue G-250) and separated on a 4–16 % NativePAGE Novex BisTris gradient gel (Life Technologies). Electrophoresis ran in three steps, i.e., using the blue cathode buffer (0.02 % Coomassie Brilliant Blue G-250) at 35 V for 70 min, and then clear cathode buffer at 25 V overnight. Finally, the voltage was increased to 200 V for 2 h. For western blotting, gels were incubated in the transfer buffer for 10 min with 0.1 % SDS, and proteins were transferred to 0.2 μm polyvinylidene difluoride (PVDF) membrane (BioRad). Western blot analysis following native gel electrophoresis was conducted using the same procedure as for SDS-PAGE (see above).

2.15. In-gel succinate dehydrogenase (SDH) activity

To assess in-gel SDH activity, 30 μg digitonin-solubilized mitochondria were mixed with 10×sample buffer containing 50 % glycerol and 0.1 % Ponceau S dye, then subjected to high-resolution clear native electrophoresis. Cathode buffer was supplemented with 0.05 % deoxycholate and 0.01 % lauryl maltoside. Electrophoresis was performed on a 4–16 % NativePAGE Novex Bis-Tris gel at 35 V for 70 min, followed by overnight running at 25 V and an additional 2 h at 200 V. To visualize the activity, gels with separated protein complexes were incubated for 20 min in an assay buffer containing 20 mM sodium succinate, 0.2 mM phenazine methosulfate, and 0.25 % nitrotetrazolium blue in 5 mM Tris-HCl (pH 7.4). The reaction was stopped using a solution of 50 % methanol and 10 % acetic acid, and gels were immediately photographed.

2.16. Succinate:quinone reductase activity

Tissue was lysed in 25 mM phosphate potassium buffer (pH 7.4) using the PBI-Shredder O2k. Protein lysates (12.5 μg) were resuspended in 100 mM phosphate buffer and transferred to a 96-well plate. The lysates were then incubated in a buffer containing 20 mM succinate, 2 μM antimycin A, 5 μM rotenone, 10 mM sodium cyanide, 50 mg/ml bovine serum albumin, and 0.015 % *w*/*v* 2,6-dichlorophenol indophenol for 5 min. The signal intensity at 600 nm was recorded for 5 min, after which 100 μM decylubiquinone was added and the reaction was recorded for 30 min. Identical measurements were performed in the presence of 20 mM malonate, and net SQR activity was obtained by subtracting the malonate-insensitive rate. Regression analysis of the linear portion of the curve was performed using GraphPad PRISM software (v.8.4.3).

2.17. Statistical analysis

The data are presented as mean values± standard error of mean (SEM). Non-parametric tests were used due to the non-normal distribution of most parameters, evaluated using Shapiro-Wilk normality test. Group differences were evaluated using Wilcoxon and Mann-Whitney test using GraphPad Prism (v.8.4.3). Significant differences were considered at $p < 0.05$.

3. Results

3.1. Clinical, pathological and molecular characteristics of RCC patients

Table 1 shows the overview of characteristics of 78 patients whose biological material, i.e. RCC tissue and adjacent healthy kidney tissue,

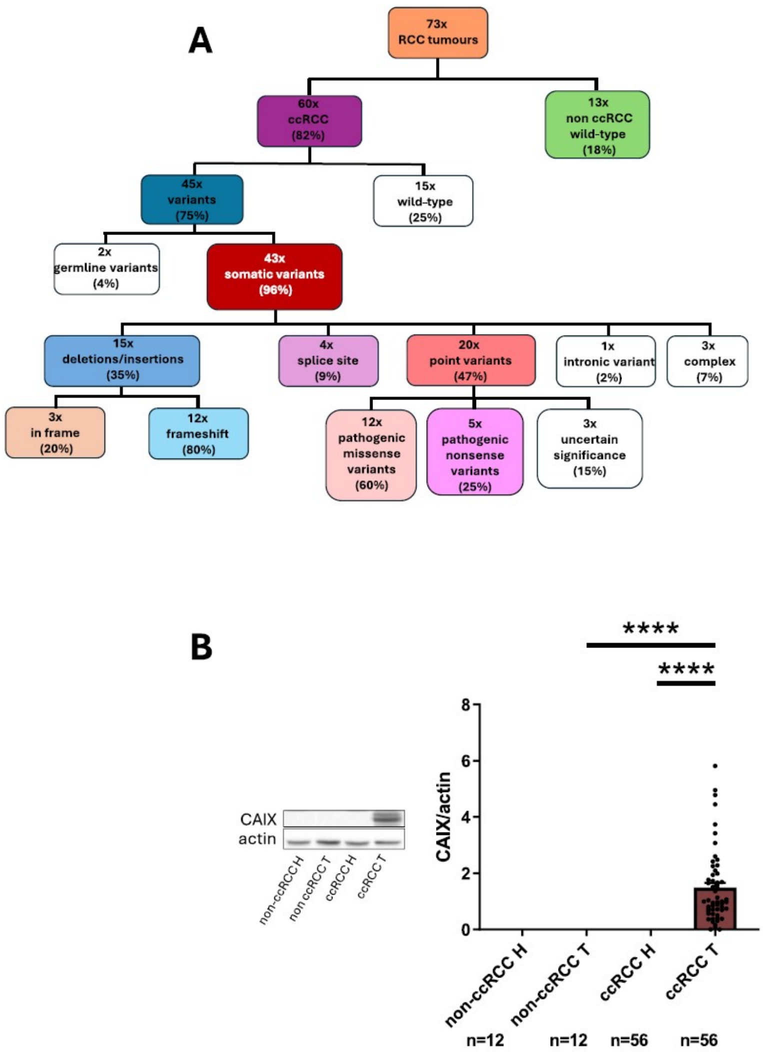

Fig. 1. ccRCC is characterized by von Hippel-Lindau gene variants and expression of carbonic anhydrase IX.
ccRCC and non-ccRCC tumour and healthy kidney tissue were evaluated for the presence of *VHL* gene variants (A). The tissue was evaluated by WB for the CAIX protein (B); lower panel, evaluation of CAIX using densitometry; upper panel, representative WB. Data are mean values ± SEM. Sample sizes are indicated within group labels. Statistical significance is indicated by asterisks, with the symbol of **** indicating $p < 0.0001$.

was used in this study. The age and gender are shown, with about 2 times more males than females. >80 % of patients had ccRCC, with the rest diagnosed with papillary or chromophobe RCC and renal oncocytoma. Concerning the grade, 68 % cases were classified as low-grade (G1/2), 23 % as high-grade (G3/4); 9 % of patients were not classified. Regarding tumour size, the majority of patients had tumours with diameters ranging from 3 to 6 cm.

Patients were classified according to the TNM staging, which includes three independent components: T (tumour size and extent), T1 includes tumours ≤7 cm in diameter confined to the kidney, T2 tumours >7 cm confined to the kidney, T3 tumours extending beyond the kidney but still within Gerota's fascia; N (lymph node involvement, N0/1), and M (distant metastasis, M0/1). Most patients had T1 and T3 tumours and only 5 patients presented with distant metastases.

Sporadic ccRCC is typified by frequent somatic *VHL* pathogenic variants. To assess this in our patient cohort, we sequenced 3 exons of the *VHL* gene from the tumour and healthy tissue of patients for the detection of variants in the gene. Fig. 1A shows that ~75 % of ccRCC tumours had *VHL* variants, while papillary or chromophobe RCC and renal oncocytoma tissue exhibited only wild-type *VHL*. We next investigated what types of pathogenic variants are present in ccRCC and found unique somatic variants in nearly all the patients including point variants, deletions/insertions and splice site variants (Fig. 1A). A detailed list of *VHL* pathogenic variants in our patient cohort, ordered by the position in the gene, is presented in Table S1. Additionally, we investigated carbonic anhydrase IX (CAIX) as a potential marker for kidney tumours at protein level. Western blot analysis revealed that CAIX is a reliable marker of ccRCC as it is not expressed in non-ccRCC tumours (Fig. 1B).

3.2. *Clear cell renal carcinoma exhibits low mitochondrial content and CII status*

As ccRCC is by far the most prevalent type of RCC, our primary focus was on patients with this tumour subtype. We first evaluated the level of mitochondria in different types of RCC as well as in the corresponding healthy kidney tissue, pooling data of non-ccRCC tumours together. Fig. 2 shows evaluation of the CIV capacity (A), mitochondrial enzyme CS activity (B), mtDNA level (C), amount of mitochondrial protein (D) and the level of the mitochondrial marker Hsp60 (E), all of which were significantly lower in tumour tissue compared to healthy kidney tissue of ccRCC patients and compared to pathological and healthy kidney tissue of non-ccRCC patients. Importantly, while there were differences between tumour tissue from ccRCC and non-ccRCC patients in all evaluated parameters, those of healthy kidney tissue from ccRCC and non-ccRCC patients were highly similar. These data indicate that tumours of non-ccRCC histotypes preserve the CIV capacity, CS enzyme activity and ETC function. Interestingly, the mtDNA/nDNA ratio (C) in non-ccRCC tumours was greater than that in corresponding healthy kidney, suggesting greater mitochondrial ETC contribution to metabolism in these tumour histotypes. Notably, we also observed low MT-CO1 IF staining in clear cell tumour tissues compared to adjacent healthy kidney tissue (Fig. 2F).

We next assessed the level and activity of CII in the same patient cohorts. Fig. 3 shows CII-dependent respiration (A), SQR activity (B), *SDHA* (C) and *SDHB* (D) transcripts, and the level of the SDHA and SDHB protein as well as the level of the SDHAF2 protein (since this assembly factor is associated with CII assembly status) (E). Similarly to the level of mitochondrial protein, we also found significantly decreased CII and in CII-related activities between ccRCC tumour tissue and non-ccRCC tumour tissue. Again, the two types of healthy kidney tissue were similar to each other (Fig. 3).

Finally, we tested the premise that mitochondrial status and CII respiration may differ in patients according to gender and age. Given the significant differences in mitochondrial parameters observed between clear cell and other histotypes and considering that clear cell is the most common histotype in both clinical practice and our cohort, combining them would introduce bias. Therefore, we focused this analysis exclusively on clear cell patients. Fig. S1 illustrates that there were no significant differences between genders, nor age groups (32–60 vs. 61–87 years of age at diagnosis) in terms of CII-dependent respiration (A), SQR activity (B), CIV capacity (C), CS activity (D) and mtDNA level (E).

3.3. *Mitochondrial content increases with the grade of ccRCC*

In the next analyses, we focused on tumour and healthy tissue from ccRCC patients according to the tumour grade using a simplified 2-tiered grading system, combining low G1/2 and high G3/4, as recommended by contemporary pathology practice [19,20]. This approach has been shown to be as effective as the traditional 4-tiered grading system in predicting cancer-specific mortality [21].

Since mitochondrial characteristics, including CIV capacity, CS activity and the level of mitochondrial proteins differed only marginally (not reaching significance) in healthy kidney tissue from G1/2 and G3/4 ccRCC patients (Fig. S2), we expressed these mitochondrial features in the corresponding tumour tissues relative to those in healthy kidney tissue. Interestingly, Fig. 4 shows that the level of mitochondria, based on the evaluated features of CIV capacity (A), CS activity (B) and isolated mitochondrial protein (C), increased with tumour grade. This indicates that with increasing grade of RCC, tumour tissue is characterized by increased mitochondrial status/function.

3.4. *Increasing grade of ccRCC is accompanied by altered CII status*

Having characterized ccRCC samples for their mitochondrial status, we decided to evaluate them also for properties of CII, relating these various analyses to corresponding healthy kidney tissue. Fig. 4 shows CII-dependent respiration (D), SQR activity (E) and SDH activity (F), related to the loading control. While there were no differences in CII-dependent respiration (D) and SQR activity (E) between G1/2 and G3/4 tissue, SDH activity (F) in isolated mitochondria was significantly decreased in G3/4 patients. We then evaluated the CII subunits SDHA and SDHB and the assembly factor SDHAF2, at the transcript (G, H, I) and protein (J, K, L, M) level, and found no significant differences (Fig. 4).

Interestingly, the pattern was quite different when we assessed CII assembly using NBGE/WB in isolated mitochondria. Fig. 4N shows that the proportion of CII_{low} sub-assemblies within total CII was higher in G3/4 ccRCC patients compared to their G1/2 counterparts and compared with healthy tissue from G3/4 patients, with the statistics shown in Fig. 4O-P. This is supported by lower level of SDHB in assembled CII compared to SDHA (Fig. 4Q), and higher level of SDHAF2 (Fig. 4R), again comparing G3/4 and G1/2 patients. Since SDHA appears to be stable within individual tissues, we used the level of this subunit as the loading control. These results show that while the function of CII in terms of CII-dependent respiration or the level of CII subunits does not change with the patient grade, the more aggressive ccRCC tumours appear to have lower level of fully assembled CII, higher level of CII sub-assemblies and lower SDH activity per mitochondrial amount.

3.5. *Tumour organoids resemble the expression pattern of mitochondrial proteins of parental tissue*

A recent approach used to recapitulate tumours in tissue culture is based on the use of organoids. We therefore prepared organoids from tumour tissue and assessed their mitochondria-linked properties, as we did for the patient tissue, with the idea that they may recapitulate properties of tissue samples shown above. To achieve this, we prepared organoids from 7 patients (patients 61, 62, 64, 68, 70, 73, 76). Fig. 5A documents successful formation of organoids from tumour tissue, clearly revealing the 3D and 2D structure of the same tissue, and indicating the presence of cell mass in tumour tissue organoids.

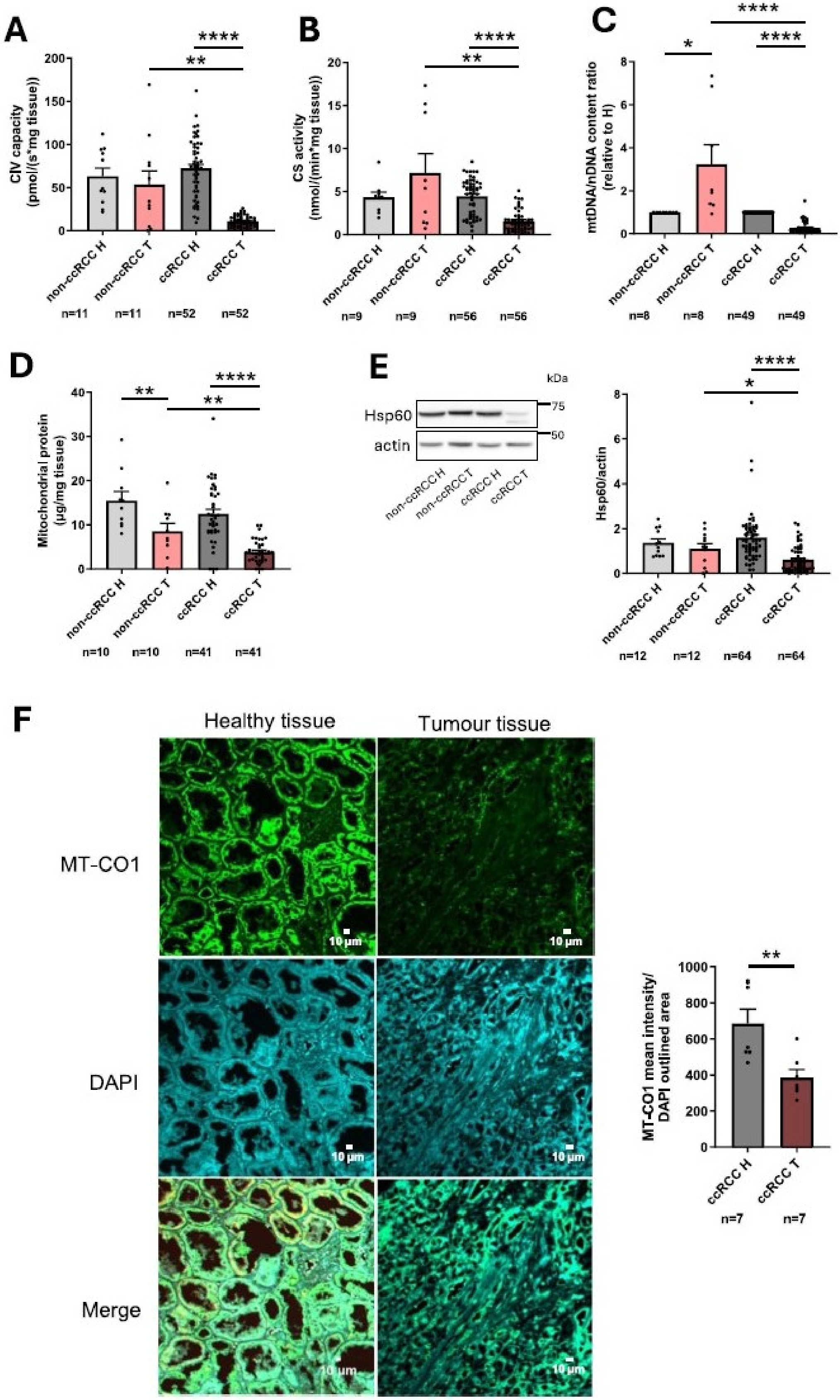

(caption on next page)

Fig. 2. ccRCC tumour tissue shows low mitochondrial expression, protein levels and function.
ccRCC and non-ccRCC tumour and healthy kidney tissue was evaluated for CIV capacity (A), CS activity (B), mtDNA/nDNA ratio (C), amount of mitochondrial protein (D), and the level of the mitochondrial marker Hsp60 (E). Panel E shows representative western blot (left), and densitometric evaluation of the level of the Hsp60 protein in patients (right). (F) Representative immunofluorescence images from paraffin-embedded sections of healthy and tumour tissue (Scale bar = 10 μm). MT-CO1 expression was analysed using ImageJ for unbiased quantification. Mean MT-CO1 intensity measured on DAPI outlined was compared between healthy and tumour tissues. The MT-CO1-stained image of tumour tissue (upper right panel) represents the same image as shown in Fig. 5I (middle left panel). Data are mean values ± SEM. Sample sizes are indicated within group labels. Statistical significance is indicated by asterisks, with the symbol of * indicating $p < 0.05$, symbol of ** $p < 0.01$, symbol of *** $p < 0.001$, symbol of **** $p < 0.0001$.

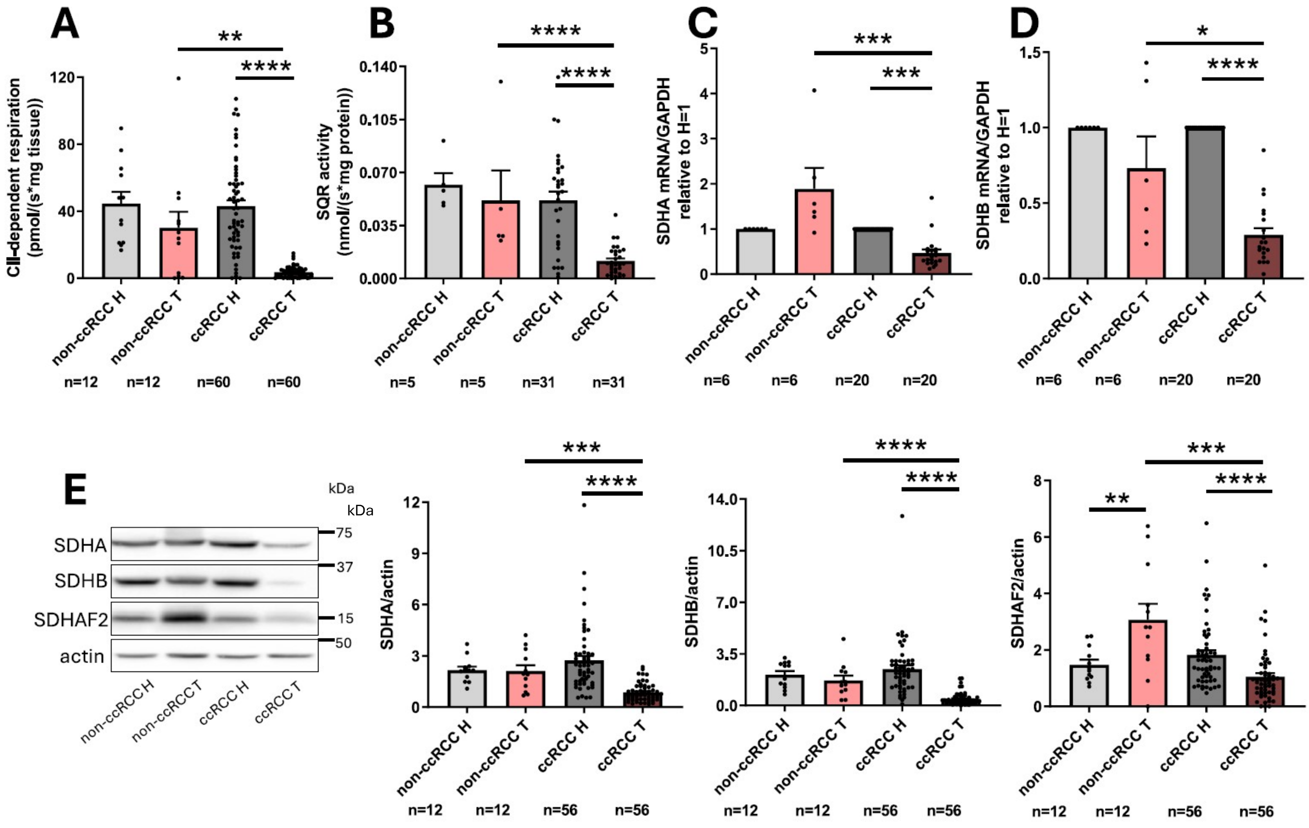

Fig. 3. Complex II function is lower in ccRCC than in other RCC types and non-tumour tissue.
ccRCC and non-ccRCC tumour and corresponding healthy kidney tissue was evaluated for CII-dependent respiration (A), SQR activity (B), *SDHA* mRNA (C), *SDHB* mRNA (D), and the level of the CII subunits SDHA and SDHB and the CII assembly factor SDHAF2 (E). Panel E shows a representative western blot (left) and densitometric evaluation (right). Data are mean values ± SEM. Sample sizes are indicated within group labels. Statistical significance is indicated by asterisks, with the symbol of * indicating $p < 0.05$, symbol of ** $p < 0.001$, symbol of **** $p < 0.0001$.

We found identical somatic *VHL* pathogenic variants in organoids and tumour tissues of the same patient (Table S1). This result underscores the reliability of the organoid model in recapitulating the *VHL* status of the original tumour. We then characterized organoids for their morphology using H&E staining and also assessed the state of CAIX, with a representative image in Fig. 5B and images for other matching tissues and organoids in Fig. S3. Of note, the CAIX staining pattern of parental tissues (low/no in healthy vs. high in tumour) is consistent with the results obtained from SDS-PAGE and western blotting of healthy and tumour tissue (Fig. 1B). By combining these two methods, we ensure both quantitative accuracy and spatial context, providing more robust and comprehensive characterization. Finally, we evaluated organoids for the level of mitochondrial proteins, including SDHA, SDHB and SDHAF2, and compared them with their levels in the corresponding tissue (Fig. 5C). We found no significant differences in the levels of Hsp60, Tomm20, SDHA, SDHB and SDHAF2 between tumour tissue and tumour organoids (Fig. 5D-H). We also performed MT-CO1 immunofluorescence staining, which revealed that the complex IV subunit, indicative of mitochondrial content, is comparable to levels observed in tumour tissue (Fig. 5I).

Collectively, these data indicate that organoids derived from kidney tumour tissue recapitulate the mitochondrial status of corresponding patient tumour tissue.

4. Discussion

In this research, we analysed healthy and tumour tissue from ccRCC and non-ccRCC patients for their mitochondrial status and the status and function of mitochondrial respiratory CII. Our study was motivated by the need to advance our understanding of mitochondrial involvement in RCC and its implications for therapeutic strategies. We were also encouraged to undertake this investigation based on our recent MitoTam clinical trial, where this mitochondrially targeted anti-cancer drug acts by disrupting mitochondrial respiratory complex I [14]. More specifically, the Phase1/1b clinical trial, which enrolled 75 patients with various diagnoses, revealed that those with RCC experienced the highest efficacy of the therapy, where 5 out of 6 RCC patients showed benefit from the treatment (either long-term stabilization or remission) [16]. All

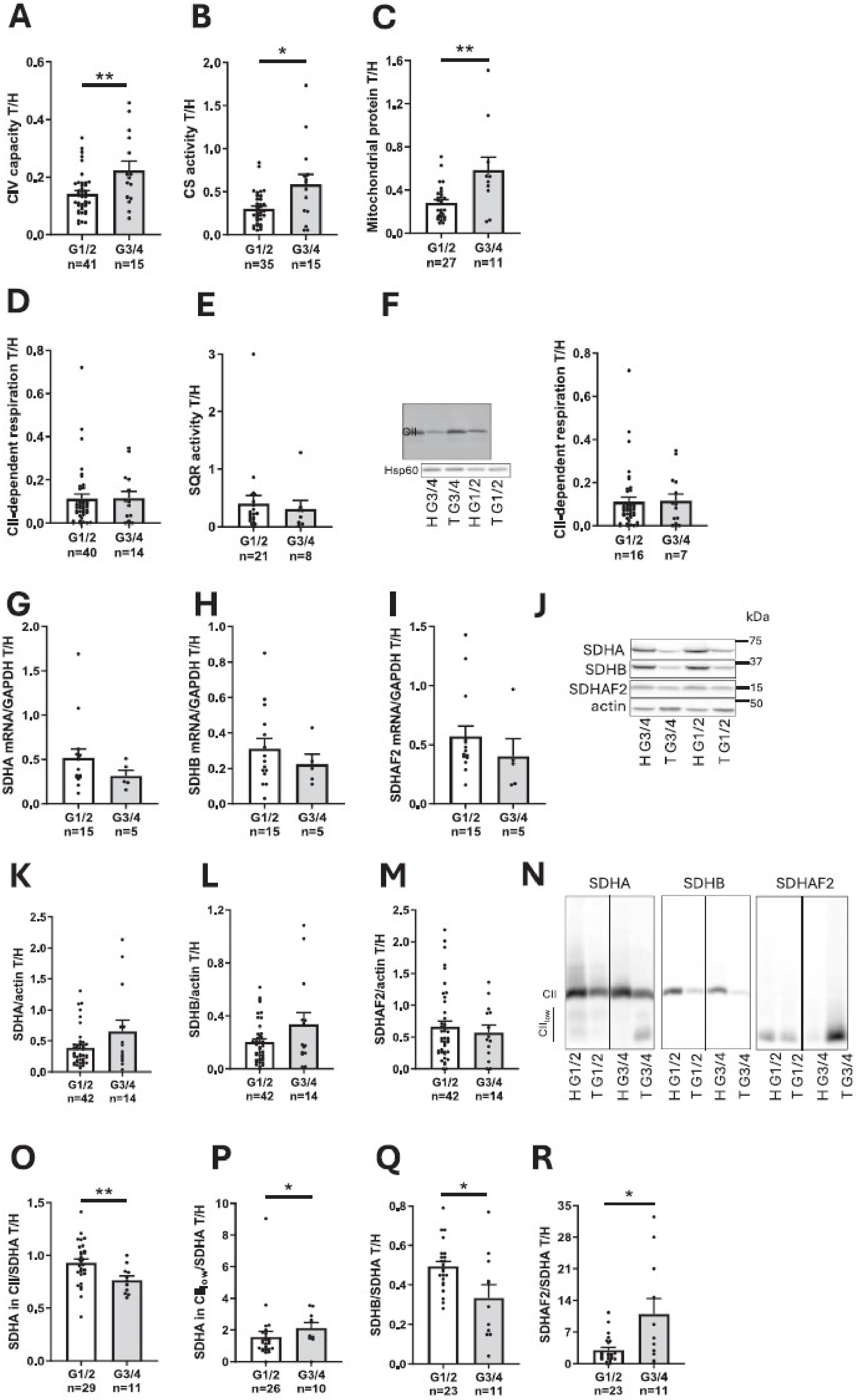

(caption on next page)

Fig. 4. Mitochondrial content, but not CII increases with tumour grade in ccRCC.
Tumour tissue from patients with Grade 1/2 and patients with Grade 3/4 was evaluated for CIV capacity (A), CS activity (B), amount of mitochondrial protein (C), CII-dependent respiration (D), SQR activity (E) and in-gel SDH activity (F), relative to healthy kidney tissue. Data in panel F are related to the loading control Hsp60. Grade 1/2 and Grade 3/4 patient tumour tissues were further evaluated for the expression of *SDHA*, *SDHB* and *SDHAF2* mRNA (G-I) and for the level of SDHA, SDHB and SDHAF2 protein using SDS-PAGE/WB (J, representative image; K-M, densitometric evaluation). Panel N shows a representative image of NBGE/WB for SDHA, SDHB and SDHAF2 in tumour and healthy tissue, and the level of SDHA in CII (O), amount of SDHA in CII_{low} (P), and the ratio of SDHB/SDHA (Q) and SDHAF2/SDHA (R). Data shown are mean values ± SEM. Sample sizes are indicated within group labels. Values of tumour tissue are related to corresponding healthy kidney tissue values. Statistical significance is indicated by asterisk, with the symbol of * indicating $p < 0.05$, symbol of ** indicating $p < 0.01$.

five patients with benefit were diagnosed with ccRCC [15]. With relevance to the effect of MitoTam on ccRCC patients via CI destabilization, it has been suggested that anomalies in CII affect CI, as shown for example in cells derived from an RCC patient with a nonsense pathogenic variant in the *SDHB* gene [17,22], or in HEK-293 SDHA KO cells [23]. Finally, RCC is known to frequently harbour anomalies in subunits and assembly factors of CII [9]. We therefore evaluated the mitochondrial status of RCC patients with a focus on CII.

VHL mutations are common in ccRCC, and we identified *VHL* variants in 75 % of our cohort of ccRCC patients, consistent with previous studies [24,25]. Our results support previous reports indicating that somatic *VHL* pathogenic variants are specific for this histotype, as we did not find *VHL* variants in other tumours [26]. Recent evidence supports the significance of *VHL*-deficient cells, suggesting that neither wild-type *VHL* nor *VHL* knockout (KO) cells alone can initiate metastasis. Instead, metastatic colonization occurs only when both cell populations co-exist, driven by secretion of pro-metastatic factors by *VHL* KO cells [27]. We identified three patients with shared splice site *VHL* pathogenic variants. Interestingly, all other sequenced tumours exhibited unique *VHL* variants (except Gln73Ter) across all three exons, without any shared variants among patients, indicating a lack of discernible hotspots. This observation aligns with findings suggesting the absence of hotspots and genotype-phenotype correlations in *VHL* pathogenic variants [28], despite ongoing efforts to predict *VHL* functional consequences using in silico methods [29]. This further emphasizes the unique properties of ccRCC.

Our results demonstrate a reduction in mitochondrial content and activity within ccRCC tumours, as evidenced by suppressed TCA cycle activity assessed by CS activity, and compromised OXPHOS function indicated by lower CIV capacity. We hypothesized that these changes in mitochondrial function could stem from a reduction in mtDNA content, and we found decreased mtDNA/nDNA ratio, which could be linked to lower expression of mtDNA-encoded genes. Indeed, low mtDNA content has been shown to downregulate ETC complex subunits, implying a direct link between mtDNA depletion and reduction in ETC proteins [30]. Therefore, a decrease in mtDNA may cause reduced OXPHOS in ccRCC.

In ccRCC, reduced mitochondrial transcription factor A (TFAM) expression results in decreased level of this mtDNA-binding protein, leading to impaired mtDNA transcription and replication [53]. Consequently, reduced TFAM-mediated regulation of mtDNA can contribute to the observed decrease in mtDNA content in ccRCC tumours. Linked to this, TFAM was previously found to be attenuated in ccRCC due to decreased level of the co-activator protein PGC1α [31]. Moreover, wild-type VHL is implicated in protecting TFAM from degradation by the LONP protease in kidney tissue, however in case of mutated *VHL*, TFAM is no longer protected from the degradation, which has negative impact on mitochondrial biogenesis in ccRCC tumour tissue [32]. This may imply that overall mitochondrial metabolism is suppressed in ccRCC tumours compared to adjacent healthy kidney tissue, explaining differences between ccRCC and other RCC histotypes. This suggests that ccRCC tumours differ from other types of RCC, which may impact their therapeutic options.

Despite impairment in mitochondrial function, ccRCC cells can sustain their energy metabolism and biosynthetic processes via glycolysis and other compensatory metabolic mechanisms, facilitating tumour growth and progression [33]. In contrast, the metabolic landscape of chromophobe or papillary RCC, due to their low frequency, remains relatively unexplored. Our study contributes to this gap by demonstrating preserved mitochondrial and CII content in chromophobe and papillary RCC. These findings contrast with an earlier report pointing to decreased ETC activity in papillary and chromophobe RCC [30], underscoring the need for further investigation of the metabolic heterogeneity in various RCC histotypes.

We observed aberrant function of CII in ccRCC tissue, manifested as reduced CII-dependent respiration. Moreover, SQR activity, critical for channeling electrons from the conversion of succinate to fumarate, catalyzed by SDH, to the ETC, was notably decreased compared to other histotypes and adjacent healthy kidney tissue. The underlying mechanism of CII inhibition in ccRCC tumours could be linked to high expression of NDUFA4L2, as this protein was previously shown to inhibit OXPHOS by targeting CI- and CII-dependent respiration in skeletal muscle and, importantly, in ccRCC [34,35]. Consequently, NDUFA4L2 may serve as a potential marker of ccRCC. Our findings collectively support the emerging understanding of ccRCC as a distinct RCC type characterized by dysregulated mitochondrial function, including CII properties.

Having observed suppression of mitochondrial metabolism in ccRCC, we decided to delve deeper into its implications for disease progression. Histological grade of tumours serves as a prognostic factor of cancer progression, with higher grade tumours often associated with increased metastatic potential. With this in mind, we compared metabolic changes of high- and low-grade tumours. We found that mitochondrial content and activity increased with grade, which is consistent with a recent study indicating re-activation of OXPHOS in metastatic tumours [36]. Interestingly, a negative correlation was found between OXPHOS levels and survival in metastatic patients [37], while another study indicated higher mtDNA content and CS activity in high-grade compared to low-grade tumours [38]. It is now considered a common characteristic that advanced stage RCCs require extensive transformation of their genomic landscape [39]. There is evidence indicating that the loss of the *SETD2* gene (coding for histone methyltransferase) is essential alongside *VHL* for tumour progression, leading to metastasis, invasion, presence of rhabdoid features, and necrosis [40]. Indeed, *SETD2* loss led to increased OXPHOS through the upregulation of PGC1α expression [41].

Surprisingly, we found no significant differences in the levels of CII subunits SDHA and SDHB, and the assembly factor SDHAF2 by SDS-PAGE/WB, or CII-dependent respiration and SQR activity between high-grade and low-grade tumours. These findings align with recent research identifying CII dysfunction as a negative prognostic indicator, with a distinct category of SDH-deficient tumours bearing mutations in CII [42–45]. Low CII activity in ccRCC is particularly noteworthy given that CII subunits, unlike those of other ETC complexes, are exclusively encoded by nuclear DNA, while mechanisms underlying the observed low level of CII function in ccRCC remain elusive. Prior studies have suggested a potential involvement of promoter methylation [46,47], direct inhibition of *SDHD* by miRNAs, and deletions of *SDHB* [9]. Intriguingly, more detailed analysis using NBGE/WB linked to CII assembly, crucial for its function, revealed decreased SDHB level and lower level of fully assembled CII in high-grade tumours, accompanied by increased levels of SDHA and SDHAF2 within the CII sub-assembly termed CII_{low}. We also found lower SDH activity in high-grade tumours. These findings suggest lower efficacy in CII assembly, possibly due to reduced SDHB availability and accumulation of CII_{low}, where

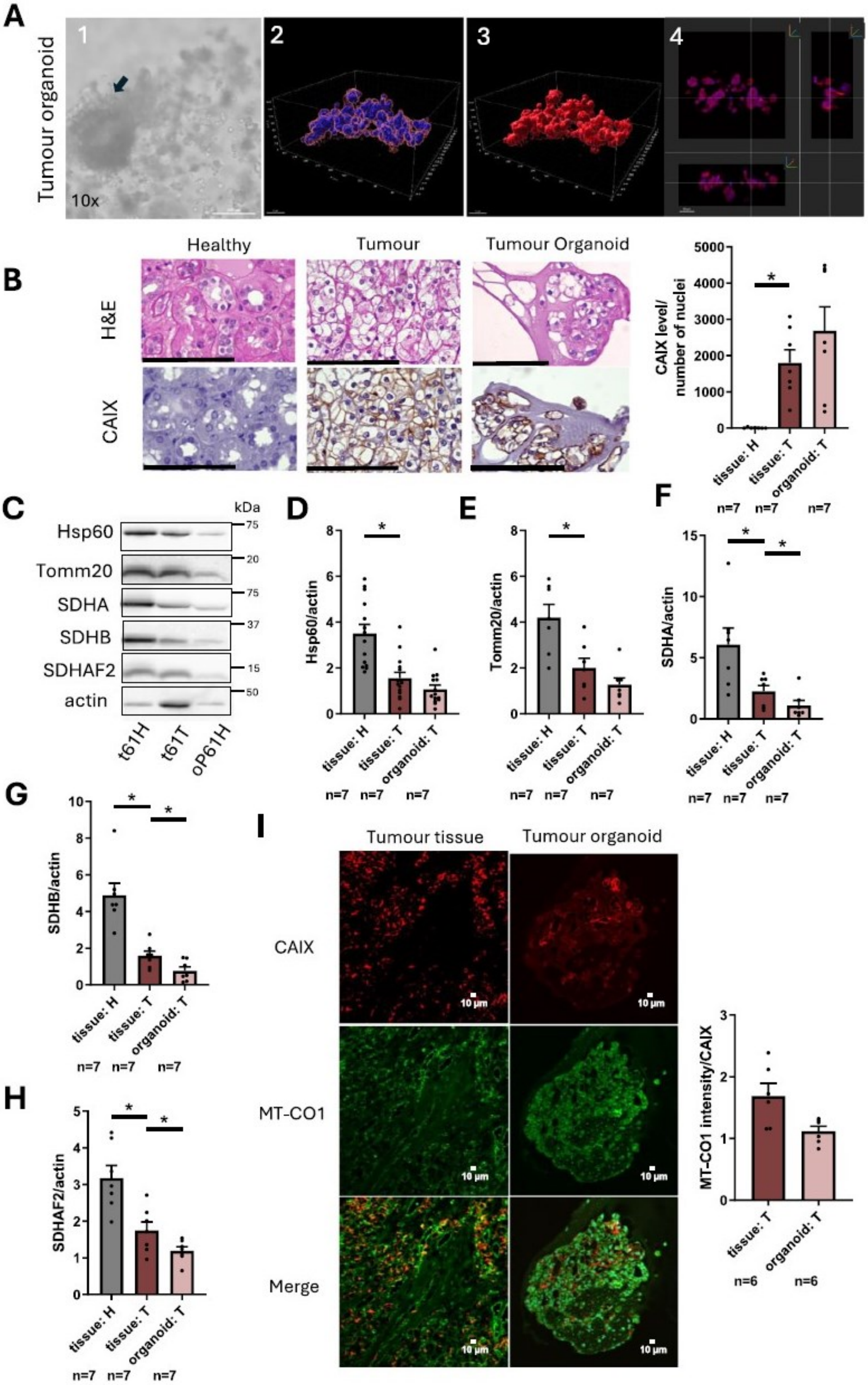

(caption on next page)

Fig. 5. Organoids from ccRCC patients recapitulate ccRCC tissue.
Phenotypic comparison of 3D organoids with parental tumour characteristics. (A1) Brightfield images (scale bar = 200 μM) of organoids derived from tumour tissue.; (A2) 3D visualization of surface-rendered nuclei and membranes in optically cleared organoids with Imaris software. Nuclei (blue); membranes (red) (A3) 3D surface rendering of membranes. (A4) orthogonal projections (scale bar = 50 μm). (B) H&E staining and CAIX staining of organoids and corresponding parental tissue from patient 76. The same H&E and CAIX images for this patient are also shown in Fig. S3. (C) WB showing levels of (D) Hsp60, (E) Tomm20, (F) SDHA, (G) SDHB, (H) SDHAF2 per the loading control actin. (I) Representative immunofluorescence images from paraffin-embedded sections of tumour tissue and tumour organoids (Scale bar = 10 μm). MT-CO1 expression was analysed using ImageJ for unbiased quantification. Mean MT-CO1 intensity measured relative to CAIX expression and was compared between tumour tissues and tumour organoids. The MT-CO1-stained image of tumour tissue (middle left panel) represents the same image as shown in Fig. 2F (upper right panel). t: tissue, o: organoid, T: tumour, H: healthy tissue. Sample sizes are indicated within group labels. Statistical significance is indicated by asterisks, with the symbol of * indicating $p < 0.05$. (For interpretation of the references to colour in this figure legend, the reader is referred to the web version of this article.)

SDHA is most likely associated with SDHAF2. Moreover, the persistence of dysfunctional CII may point to secondary function of the CII_{low} subassembly, potentially aiding tumour progression/metastasis via distinct mechanisms that are not clear at present.

We have yet to determine the underlying cause of the simultaneous upregulation of mitochondrial function and imbalance in CII assembly in high-grade ccRCC tumours. Our investigation implicates CII_{low} as a potential negative prognostic marker in ccRCC, reflecting its role in promoting tumorigenesis and metastasis.

Models that recapitulate patient tumours are scarce and not highly reliable. A recent and potentially promising approach is the use of organoids derived from tumours. Here, we show successful preparation of organoids from tumour tissue of seven ccRCC patients, with these organoids preserving the histological architecture of the parental tissue. They presented as small, cell-dense, non-cystic structures without distinct organization and morphology, as shown previously [48].

To determine whether phenotypic features found in tumour tissue are retained in vitro, we characterized the organoids. The search for a reliable marker of RCC remains challenging. We found that CAIX is expressed in ccRCC tumours, but not in papillary and chromophobe RCC or renal oncocytoma, as shown previously [49]. This suggests that ccRCC tumours likely reflect a pseudo-hypoxic environment controlled by HIF1α signaling. CAIX plays a key role in adapting to hypoxia by regulating pH through converting carbon dioxide to bicarbonate and protons, enabling cancer cells to survive and thrive in low-oxygen conditions [50]. Our tumour organoids resemble the parental tumour tissue in that they are positive for CAIX, indicating preservation of this pseudo-hypoxic environment marker, as supported by the literature [51]. To test whether RCC organoids preserve the *VHL* variants of their parental tumours, amplicon sequencing was performed on seven established RCC organoids and their matching tumour samples. The shared known somatic variants in *VHL* found in the tumour tissues were conserved in all corresponding RCC organoids. These results confirm previous reports of preservation of *VHL* mutations in the majority of organoids derived from the respective primary tumours [52].

Regarding mitochondrial and CII properties, we found that organoids derived from tumours were similar to parental tumours in terms of decreased mitochondrial content and diminished CII properties. This is the first study to examine CII properties in RCC-derived organoids, highlighting their potential as a model of ccRCC. Additionally, these organoids could serve as valuable tools for mitochondrial research or pharmacological screening.

5. Conclusion

In summary, we demonstrate that decreased CII activity is a common feature in ccRCC, with adverse functional and prognostic implications. Additionally, elucidating the functional significance of altered CII assembly dynamics observed in high-grade tumours could provide valuable insights into tumour progression. While the precise mechanism(s) underlying this phenomenon remain elusive, our findings suggest a potential role for CII_{low} in driving tumorigenesis and metastasis. Overall, our findings contribute to deeper understanding of metabolic reprogramming in ccRCC and pave the way for future research aimed at identifying potential treatment strategies and improving patient outcomes, implying the use of tumour-derived organoids.

Supplementary data to this article can be found online at https://doi.org/10.1016/j.bbadis.2024.167556.

Funding

This work was supported in part by grants from Czech Health Foundation NU21-03-00545 to J.N., NU23-03-00226 to S.D., NU20-03-00309 to K.K., from Czech Science Foundation 23-05303S to S.Bo, and from MH CZ-DRO (Institute of Endocrinology – EÚ, 00023761) to J.V.

CRediT authorship contribution statement

Sona Miklovicova: Writing – review & editing, Writing – original draft, Visualization, Validation, Investigation, Formal analysis, Data curation, Conceptualization. **Luca Volpini:** Writing – review & editing, Writing – original draft, Methodology, Investigation, Conceptualization. **Ondrej Sanovec:** Validation, Methodology, Investigation. **Federica Monaco:** Investigation, Formal analysis, Data curation. **Katerina Hadrava Vanova:** Writing – review & editing, Writing – original draft, Resources, Methodology. **Jaromir Novak:** Visualization, Validation, Methodology, Investigation. **Stepana Boukalova:** Writing – review & editing, Writing – original draft, Supervision, Investigation, Conceptualization. **Renata Zobalova:** Methodology, Investigation, Data curation. **Petr Klezl:** Validation, Resources, Data curation. **Marco Tomasetti:** Supervision. **Vladimir Bobek:** Validation, Resources, Data curation. **Vojtech Fiala:** Validation, Resources, Data curation. **Josef Vcelak:** Software, Methodology, Investigation, Formal analysis, Data curation. **Lory Santarelli:** Validation, Supervision, Resources. **Zuzana Bielcikova:** Writing – review & editing, Writing – original draft, Resources, Investigation, Formal analysis, Conceptualization. **Katerina Komrskova:** Writing – review & editing, Writing – original draft, Supervision, Resources. **Katarina Kolostova:** Writing – review & editing, Writing – original draft, Validation, Resources, Data curation. **Karel Pacak:** Writing – review & editing, Writing – original draft, Supervision, Resources. **Sarka Dvorakova:** Writing – review & editing, Writing – original draft, Supervision, Project administration, Funding acquisition, Data curation, Conceptualization. **Jiri Neuzil:** Writing – review & editing, Writing – original draft, Supervision, Resources, Funding acquisition, Conceptualization.

Declaration of competing interest

We declare here that no co-author has any clash of interest.

Acknowledgements

We thank Prof Michael V. Berridge (Malaghan Institute for Medical Research, Wellington, New Zealand) for critical reading and editing this manuscript.

Data availability

Data will be made available on request.

References

[1] U. Capitanio, et al., Epidemiology of renal cell carcinoma, Eur. Urol. 75 (1) (2019) 74–84, https://doi.org/10.1016/j.eururo.2018.08.036.

[2] R.L. Siegel, K.D. Miller, A. Jemal, Cancer statistics, 2020, CA Cancer J. Clin. 70 (1) (2020) 7–30, https://doi.org/10.3322/caac.21590.

[3] D. Lindgren, et al., Cell-type-specific gene programs of the normal human nephron define kidney cancer subtypes, Cell Rep. 20 (6) (2017) 1476–1489, https://doi.org/10.1016/j.celrep.2017.07.043.

[4] Y. Sato, et al., Integrated molecular analysis of clear-cell renal cell carcinoma, Nat. Genet. 45 (8) (2013) 860–867, https://doi.org/10.1038/ng.2699.

[5] M. Ivan, et al., HIFα targeted for VHL-mediated destruction by proline hydroxylation: implications for O2 sensing, Science 292 (5516) (2001) 464–468, https://doi.org/10.1126/science.1059817.

[6] B.I. Rini, S.C. Campbell, B. Escudier, Renal cell carcinoma, Lancet 373 (2009) 1119–1151, https://doi.org/10.1016/S0140.

[7] S. Fuhrman, L. Lasky, C. Limas, Prognostic significance of morphologic parameters in renal cell carcinoma, Am. J. Surg. Pathol. 6 (7) (1982) 655–663.

[8] H. Moch, A.L. Cubilla, P.A. Humphrey, V.E. Reuter, T.M. Ulbright, The 2016 WHO classification of tumours of the urinary system and male genital organs—part a: renal, penile, and testicular tumours, Eur Urol 70 (1) (2016) 93–105, https://doi.org/10.1016/j.eururo.2016.02.029.

[9] R.K. Aggarwal, et al., Functional succinate dehydrogenase deficiency is a common adverse feature of clear cell renal cancer 118 (2021) 2106947118, https://doi.org/10.1073/pnas.2106947118/-/DCSupplemental.

[10] T.M. Iverson, P.K. Singh, G. Cecchini, An evolving view of complex II—noncanonical complexes, megacomplexes, respiration, signaling, and beyond,J. Biol. Chem. 299 (6) (2023), https://doi.org/10.1016/j.jbc.2023.104761.

[11] A. Bezawork-Geleta, J. Rohlena, L. Dong, K. Pacak, J. Neuzil, Mitochondrial Complex II: At the Crossroads, Trends Biochem. Sci. 42 (4) (2017), https://doi.org/10.1016/j.tibs.2017.01.003.

[12] P. Sharma, et al., Disordered-to-ordered transitions in assembly factors allow the complex II catalytic subunit to switch binding partners, Nat. Commun. 15 (1) (2024), https://doi.org/10.1038/s41467-023-44563-7.

[13] A. Bezawork-Geleta, et al., Alternative assembly of respiratory complex II connects energy stress to metabolic checkpoints, Nat. Commun. 9 (1) (2018), https://doi.org/10.1038/s41467-018-04603-z.

[14] K. Rohlenova, et al., Selective disruption of respiratory supercomplexes as a new strategy to suppress Her2high breast cancer, Antioxid. Redox Signal. 26 (2) (2017) 84–103, https://doi.org/10.1089/ars.2016.6677.

[15] Z. Bielcikova, et al., Mitochondrially targeted tamoxifen as anticancer therapy: case series of patients with renal cell carcinoma treated in a phase I/Ib clinical trial, Ther. Adv. Med. Oncol. 15 (2023), https://doi.org/10.1177/17588359231197957.

[16] Z. Bielcikova, et al., Mitochondrially targeted tamoxifen in patients with metastatic solid tumours: an open-label, phase I/Ib single-Centre trial, EClinicalMedicine 57 (2023), https://doi.org/10.1016/j.eclinm.2023.101873.

[17] N. Saxena, et al., SDHB-deficient cancers: the role of mutations that impair iron sulfur cluster delivery, J. Natl. Cancer Inst. 108 (1) (2016), https://doi.org/10.1093/jnci/djv287.

[18] K. Chung, et al., Structural and molecular interrogation of intact biological systems, Nature 497 (7449) (2013) 332–337, https://doi.org/10.1038/nature12107.

[19] J. Ding, et al., CT-based radiomic model predicts high grade of clear cell renal cell carcinoma, Eur. J. Radiol. 103 (2018) 51–56, https://doi.org/10.1016/j.ejrad.2018.04.013.

[20] J. Shu, et al., Clear cell renal cell carcinoma: CT-based radiomics features for the prediction of Fuhrman grade, Eur. J. Radiol. 109 (2018) 8–12, https://doi.org/10.1016/j.ejrad.2018.10.005.

[21] A. Becker, et al., Critical analysis of a simplified Fuhrman grading scheme for prediction of cancer specific mortality in patients with clear cell renal cell carcinoma - impact on prognosis, Eur. J. Surg. Oncol. 42 (3) (2016) 419–425, https://doi.org/10.1016/j.ejso.2015.09.023.

[22] M.L. Hart, et al., Mitochondrial redox adaptations enable alternative aspartate synthesis in SDH-deficient cells, Elife 12 (2023), https://doi.org/10.7554/elife.78654.

[23] K. Čunátová, et al., Mitochondrial translation is the primary determinant of secondary mitochondrial complex I deficiencies, iScience (2024) 110560, https://doi.org/10.1016/j.isci.2024.110560.

[24] M.L. Nickerson, et al., Improved identification of von Hippel-Lindau gene alterations in clear cell renal tumors, Clin. Cancer Res. 14 (15) (2008) 4726–4734, https://doi.org/10.1158/1078-0432.CCR-07-4921.

[25] A.C. Young, et al., Analysis of VHL gene alterations and their relationship to clinical parameters in sporadic conventional renal cell carcinoma, Clin. Cancer Res. 15 (24) (2009) 7582–7592, https://doi.org/10.1158/1078-0432.CCR-09-2131.

[26] A.A. Batavia, P. Schraml, H. Moch, Clear cell renal cell carcinoma with wild-type von Hippel-Lindau gene: a non-existent or new tumour entity? Histopathology 74 (1) (2019) https://doi.org/10.1111/his.13749.

[27] J. Hu, et al., Tumor heterogeneity in VHL drives metastasis in clear cell renal cell carcinoma, Signal Transduct. Target. Ther. 8 (1) (2023), https://doi.org/10.1038/s41392-023-01362-2.

[28] P. Hudler and M. Urbancic, The Role of VHL in the Development of von Hippel-Lindau Disease and Erythrocytosis, Genes (Basel), vol. 13, no. 2, doi:https://doi.org/10.3390/genes13020362.

[29] A. Serghini, et al., Characterizing and predicting ccRCC-causing missense mutations in Von Hippel-Lindau disease, Hum. Mol. Genet. 33 (3) (2024) 224–232, https://doi.org/10.1093/hmg/ddad181.

[30] Y. Xiao, et al., Decreased mitochondrial DNA content drives OXPHOS dysregulation in chromophobe renal cell carcinoma, Cancer Res. 80 (18) (2020) 3830–3840, https://doi.org/10.1158/0008-5472.CAN-20-0754.

[31] E.L. LaGory, et al., Suppression of PGC-1α is critical for reprogramming oxidative metabolism in renal cell carcinoma, Cell Rep. 12 (1) (2015) 116–127, https://doi.org/10.1016/j.celrep.2015.06.006.

[32] S. Li, et al., Impaired oxygen-sensitive regulation of mitochondrial biogenesis within the von Hippel–Lindau syndrome, Nat. Metab. 4 (6) (2022) 739–758, https://doi.org/10.1038/s42255-022-00593-X.

[33] H. Zhu, X. Wang, S. Lu, K. Ou, Metabolic reprogramming of clear cell renal cell carcinoma, Frontiers Media S.A. (2023), https://doi.org/10.3389/fendo.2023.1195500.

[34] Z. Liu, et al., Mitochondrial NDUFA4L2 is a novel regulator of skeletal muscle mass and force, FASEB J. 35 (12) (2021), https://doi.org/10.1096/fj.202100066R.

[35] J.M. Kubala, et al., NDUFA4L2 reduces mitochondrial respiration resulting in defective lysosomal trafficking in clear cell renal cell carcinoma, Cancer Biol. Ther. 24 (1) (2023), https://doi.org/10.1080/15384047.2023.2170669.

[36] D. Bezwada, et al., Mitochondrial complex I promotes kidney cancer metastasis, Nature (2024), https://doi.org/10.1038/s41586-024-07812-3.

[37] J. Tian, et al., Targeting oxidative phosphorylation to increase the efficacy of immune-combination therapy in renal cell carcinoma, J. Immunother. Cancer 12 (2) (2024) e008226, https://doi.org/10.1136/jitc-2023-008226.

[38] D. Meierhofer, et al., Decrease of mitochondrial DNA content and energy metabolism in renal cell carcinoma, Carcinogenesis 25 (6) (2004) 1005–1010, https://doi.org/10.1093/carcin/bgh104.

[39] F. Martínez-Jiménez, et al., Pan-cancer whole-genome comparison of primary and metastatic solid tumours, Nature 618 (7964) (2023) 333–341, https://doi.org/10.1038/s41586-023-06054-z.

[40] K. Takeda, S. Bastacky, R. Dhir, M. Mohebnasab, G.M. Quiroga-Garza, Morphological characteristics of SETD2-mutated locally advanced clear cell renal cell carcinoma: comparison with BAP1-mutated clear cell renal cell carcinoma, Ann. Diagn. Pathol. 68 (2024), https://doi.org/10.1016/j.anndiagpath.2023.152223.

[41] J. Liu, et al., Loss of SETD2 induces a metabolic switch in renal cell carcinoma cell lines toward enhanced oxidative phosphorylation, J. Proteome Res. 18 (1) (2019) 331–340, https://doi.org/10.1021/acs.jproteome.8b00628.

[42] N.J. Coffey, M.C. Simon, Metabolic alterations in hereditary and sporadic renal cell carcinoma, Nature Research (2024), https://doi.org/10.1038/s41581-023-00800-2.

[43] K.M. Cornejo, et al., Succinate dehydrogenase B: a new prognostic biomarker in clear cell renal cell carcinoma, Hum. Pathol. 46 (6) (2015) 820–826, https://doi.org/10.1016/j.humpath.2015.02.013.

[44] J.B. Neves, et al., Defining the origin, evolution, and immune composition of SDH-deficient renal cell carcinoma, iScience 25 (11) (2022), https://doi.org/10.1016/j.isci.2022.105389.

[45] C.J. Ricketts, et al., Kidney tumors associated with germline mutations of FH and SDHB show a CpG island methylator phenotype (CIMP), PloS One 17 (12 December) (2022), https://doi.org/10.1371/journal.pone.0278108.

[46] Z. Fang, Q. Sun, H. Yang, J. Zheng, SDHB suppresses the tumorigenesis and development of ccRCC by inhibiting glycolysis, Front. Oncol. 11 (2021), https://doi.org/10.3389/fonc.2021.639408.

[47] J. Yang, et al., Functional deficiency of succinate dehydrogenase promotes tumorigenesis and development of clear cell renal cell carcinoma through weakening of ferroptosis, Bioengineered 13 (4) (2022) 11187–11207, https://doi.org/10.1080/21655979.2022.2062537.

[48] C. Calandrini, et al., An organoid biobank for childhood kidney cancers that captures disease and tissue heterogeneity, Nat. Commun. 11 (1) (Dec. 2020), https://doi.org/10.1038/s41467-020-15155-6.

[49] A. Luong-Player, H. Liu, H.L. Wang, F. Lin, Immunohistochemical reevaluation of carbonic anhydrase IX (CA IX) expression in tumors and normal tissues, Am. J. Clin. Pathol. 141 (2) (2014) 219–225, https://doi.org/10.1309/AJCPVJDS28KNYZLD.

[50] H.M. Becker, Carbonic Anhydrase IX and Acid Transport in Cancer, Springer Nature, 2020, https://doi.org/10.1038/s41416-019-0642-z.

[51] Y. Xue, et al., Patient-derived organoids potentiate precision medicine in advanced clear cell renal cell carcinoma, Precis. Clin. Med. 5 (4) (2022), https://doi.org/10.1093/pcmedi/pbac028.

[52] Z. Li, et al., Patient-derived renal cell carcinoma organoids for personalized cancer therapy, Clin. Transl. Med. 12 (7) (2022), https://doi.org/10.1002/ctm2.970.

[53] C. Kukat, et al., Cross-strand binding of TFAM to a single mtDNA molecule forms the mitochondrial nucleoid, Proc Natl Acad Sci U S A 12 (36) (2015) 11288–11293, https://doi.org/10.1073/pnas.1512131112.

nature communications

Article

https://doi.org/10.1038/s41467-023-44563-7

Disordered-to-ordered transitions in assembly factors allow the complex II catalytic subunit to switch binding partners

Received: 29 November 2022

Accepted: 19 December 2023

Pankaj Sharma[1], Elena Maklashina[2,3], Markus Voehler[4,5], Sona Balintova[6,7], Sarka Dvorakova[6], Michal Kraus[6], Katerina Hadrava Vanova[6,8], Zuzana Nahacka[6], Renata Zobalova[6], Stepana Boukalova[6], Kristyna Cunatova[9], Tomas Mracek[9], Hans K. Ghayee[10], Karel Pacak[8], Jakub Rohlena[6], Jiri Neuzil[6,7,11,12], Gary Cecchini[2,3] & T. M. Iverson[1,5,13,14]

Complex II (CII) activity controls phenomena that require crosstalk between metabolism and signaling, including neurodegeneration, cancer metabolism, immune activation, and ischemia-reperfusion injury. CII activity can be regulated at the level of assembly, a process that leverages metastable assembly intermediates. The nature of these intermediates and how CII subunits transfer between metastable complexes remains unclear. In this work, we identify metastable species containing the SDHA subunit and its assembly factors, and we assign a preferred temporal sequence of appearance of these species during CII assembly. Structures of two species show that the assembly factors undergo disordered-to-ordered transitions without the appearance of significant secondary structure. The findings identify that intrinsically disordered regions are critical in regulating CII assembly, an observation that has implications for the control of assembly in other biomolecular complexes.

Respiratory complex II (CII; succinate dehydrogenase, SDH) connects the Krebs cycle with oxidative phosphorylation, making it a master regulator of cell metabolism[1–3]. CII also controls cell fate by regulating succinate signaling, aerobic respiration, and hypoxic metabolism[1–3]. These functions affect a range of human diseases[4,5]; most notably CII activity suppresses tumor formation[6,7]. CII activity can be regulated in many ways. For example, it has long been known that substrate-level inhibition of succinate oxidation by oxaloacetate provides feedback control in the Krebs cycle[8–10]. Covalent inhibition of the same succinate-binding site by the small molecule 3-nitropropionate induces cell death in striatal neurons and leads to neurodegeneration[11,12]. Some mutations of the catalytic SDHA subunit of CII, which oxidizes succinate[4,13–15], also correlate with a neurodegenerative clinical presentation.

---

[1]Department of Pharmacology, Vanderbilt University, Nashville, TN 37232, USA. [2]Molecular Biology Division, San Francisco VA Health Care System, San Francisco, CA 94121, USA. [3]Department of Biochemistry & Biophysics, University of California, San Francisco, CA 94158, USA. [4]Department of Chemistry Vanderbilt University, Nashville, TN 37232, USA. [5]Center for Structural Biology Vanderbilt University, Nashville, TN 37232, USA. [6]Institute of Biotechnology, Czech Academy of Sciences, 252 50, Prague-West, Czech Republic. [7]Faculty of Science, Charles University, 128 00, Prague 2, Czech Republic. [8]Eunice Kennedy Shriver National Institute of Child Health and Human Development, National Institutes of Health, Bethesda, MD 20814, USA. [9]Institute of Physiology, Czech Academy of Sciences, Prague 4, 142 20, Prague, Czech Republic. [10]Department of Medicine, Division of Endocrinology & Metabolism, University of Florida College of Medicine and Malcom Randall, VA Medical Center, Gainesville, FL 32608, USA. [11]School of Pharmacy and Medical Science, Griffith University, Southport, QLD 4222, Australia. [12]1st Faculty of Medicine, Charles University, 128 00, Prague 2, Czech Republic. [13]Department of Biochemistry, Vanderbilt University, Nashville, TN 37232, USA. [14]Vanderbilt Institute of Chemical Biology, Vanderbilt University, Nashville, TN 37232, USA.
e-mail: j.neuzil@griffith.edu.au; jiri.neuzil@ibt.cas.cz; Gary.Cecchini@ucsf.edu; tina.iverson@vanderbilt.edu

Although data are limited[16–18], the synthesis of a number of findings suggests that CII activity is regulated at the level of assembly in some biological situations. This may be a relatively complex process as mature CII contains four protein subunits (SDHA, SDHB, SDHC, and SDHD) and houses five permanently-associated cofactors (covalent FAD, [2Fe-2S], [4Fe-4S], and [3Fe-4S] clusters, and integral-membrane *b* heme)[19]. Potentially to allow for rapid onset of CII activity, CII assembly intermediates appear to be stable and can accumulate in cells. For example, the SDHA subunit can accumulate with one or more of its assembly factors as a long-lived complex of ~100 kDa, also referred to as $\mathrm{CII_{low}}$, under conditions with stalled CII assembly[20]. In addition, dynamic disassembly of mature CII induces the appearance of a ~100 kDa species containing unassembled SDHA during macrophage activation[21] and as a response to acute ischemia, such as observed in heart attack and stroke[22–24]. In each of these cases, the removal of SDHA from assembled CII is expected to affect cellular succinate oxidation, which in turn regulates succinate signaling and metabolism. Understanding the nature of these stable intermediates and how SDHA transitions between them can therefore provide insight into the shifts in metabolism that hallmark diseases and biological states associated with changes in CII activity.

In eukaryotes, CII biogenesis involves at least four SDH assembly factors (SDHAFs)[25–30]. Individuals with mutations in these SDHAFs may exhibit pathologies associated with CII insufficiency[26–28,31]. Of these, SDHAF2 and SDHAF4 both interact directly with the catalytic SDHA subunit of CII[28,32]. In conjunction with the FAD cofactor and a small molecule dicarboxylate[32,33], these assembly factors are proposed to be involved in post-folding SDHA maturation events including correct cofactor association[26,28,32,34] (Fig. 1). SDHAF2 enhances covalent FAD attachment to SDHA[26,32], but the role of SDHAF4 is somewhat cryptic. Nevertheless, loss of SDHAF4 reduces CII assembly, promotes mitophagy, induces dilated cardiopathy in mice[35], and induces neurodegeneration in drosophila[28]. Conversely, SDHAF4 appears to be downregulated as a response to pathological stress in human cardiac muscle[35].

Synthesis of past work suggests that SDHAF2 and SDHAF4 each form binary interactions with SDHA and that they likely bind in a defined temporal order. For example, SDHAF2 increases the affinity of SDHA for dicarboxylate and FAD[33] suggesting that SDHAF2 may bind before these small molecules. SDHAF2 and dicarboxylate enhance covalent flavinylation[32], while SDHAF4 binds SDHA that contains covalent FAD in yeast[28], implying that the action of SDHAF4 follows that of SDHAF2.

In this study, we combined cellular studies, structural studies, and in vitro biochemistry to identify metastable soluble species that contain SDHA, SDHAF2, and SDHAF4. Changes in the intrinsic disorder of the SDHAF2 and SDHAF4 assembly factors are observed across the different complexes, and we show that the disordered regions of these assembly factors are critical for the transfer of SDHA between complexes. Structural parallels found via retrospective analysis of other systems suggest that changes in intrinsic disorder may guide the assembly or disassembly of complexes in many systems.

Results

SDHA-SDHAF2 is the first protein-protein complex formed during SDHA maturation

To interrogate the possibilities for SDHA handling, we systematically evaluated pair-wise interactions between apo-SDHA, and either SDHAF2 or SDHAF4 using pull-down assays. These assays were also designed to determine whether the cofactor status of SDHA impacts the ability of SDHA to associate with each of these assembly factors.

Using recombinant proteins and beginning with the SDHA-SDHAF2 interaction, we found that SDHAF2 bound robustly to SDHA regardless of the presence and covalent status of FAD (Fig. 2a, lanes 1–3). This suggests that SDHAF2 binding is independent of the status of the FAD cofactor. In contrast, a similar experiment showed that SDHAF4 did not bind detectably to apo-SDHA (Fig. 2b, lane 1), and only weakly associated with SDHA with non-covalent FAD (Fig. 2b, lane 2) and SDHA with covalent FAD (Fig. 2b, lane 3). We also tested if SDHAF2 and SDHAF4 can interact directly. However, as shown in Supplementary Fig. 1 (lanes 2–4), the amount of SDHAF2 in the pull-down (Supplementary Fig. 1, lanes 2–4) is equivalent to the amount pulled-down in a negative control (Supplementary Fig. 1, lane 4). This finding suggests that the two assembly factors do not directly interact.

Consistent with a very strong binding of SDHAF2 and weak or no binding of SDHAF4 to SDHA, when apo-SDHA is exposed to a mixture of SDHAF2 and SDHAF4, only SDHAF2 binding is detectable (Fig. 2c, lane 1). The presence of non-covalent FAD has no effect on this binding pattern (Fig. 2c, lane 2). Interestingly, when SDHA contains covalent FAD, the mixture of SDHAF2 and SDHAF4 showed a reverse pattern, where SDHAF4 bound robustly and the amount of bound SDHAF2 was significantly reduced (Fig. 2c, lane 3).

Placing these findings in the context of past work, which shows that SDHAF2 enhances covalent flavin attachment to SDHA and that SDHAF4 binds to flavinylated SDHA[28,32], the most likely interpretation of these pair-wise interaction studies is that the assembly factors each bind to SDHA in a defined temporal sequence. First, SDHAF2 and fumarate bind to SDHA, which stimulates the covalent attachment of FAD to SDHA[32,33]. Subsequently, SDHAF4 binds to the holo-SDHA-AF2 complex and displaces SDHAF2. An alternative interpretation is that fumarate itself affects SDHA association with the assembly factors. To test this, we pre-formed the SDHA-AF2 complex with covalent FAD and evaluated the impact of adding SDHAF4. Consistent with a mechanism where the assembly factors bind sequentially, SDHAF4 bound robustly to SDHA and significantly displaced SDHAF2 independent of the presence of fumarate (Fig. 2d).

If the in vitro work correctly predicts this sequence of events in cells, we would anticipate that cells lacking SDHAF4 would have stalled CII assembly and would accumulate the SDHA-AF2 complex. To test this, we developed duplicate $\mathrm{SDHAF4^{KO}}$ clones ($\mathrm{SDHAF4^{KO36}}$ and $\mathrm{SDHAF4^{KO81}}$) in a human adrenal pheochromocytoma cell line

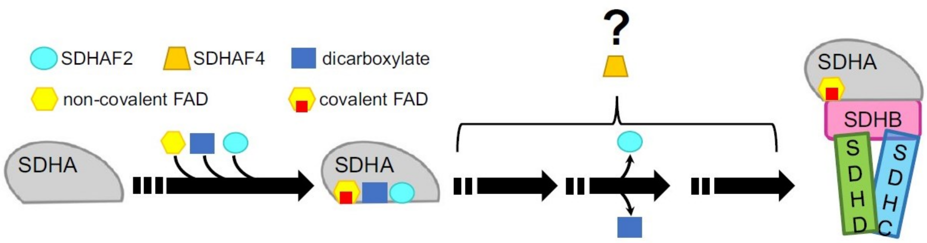

Fig. 1 | Simplified scheme of SDHA maturation. SDHA maturation requires FAD, dicarboxylate, SDHAF2, and SDHAF4. Each of these molecules makes binary interactions with SDHA, but the exact sequence of these binary interactions is not known. SDHA must have covalent FAD attached before it assembles into CII if the final protein complex is to be fully functional[26,74,75].

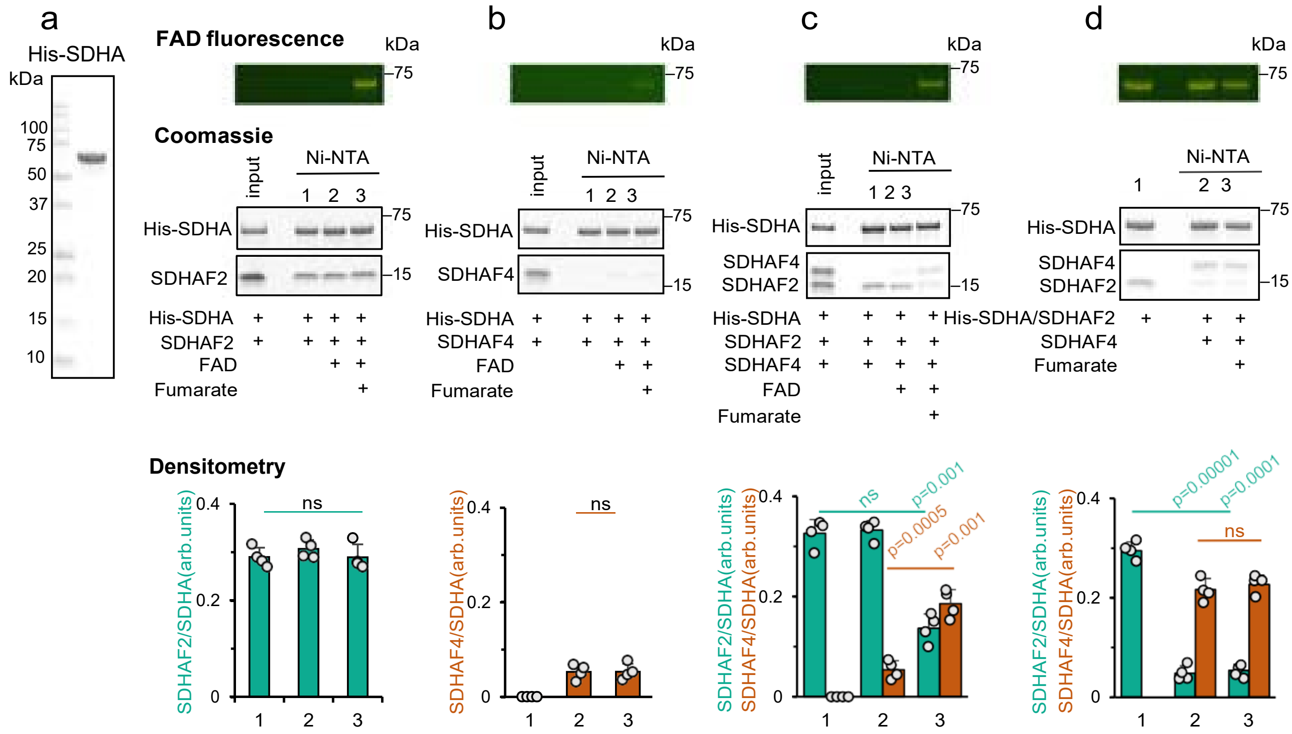

Fig. 2 | Pairwise interactions between SDHA, SDHAF2, and SDHAF4. The interaction of His-SDHA (2.6 µM) with SDHAF2 (6.4 µM) and SDHAF4 (8 µM) was evaluated by using a Ni-NTA pull-down assay. SDHA was tested in several of its forms: apo-SDHA, SDHA with bound non-covalent FAD, and holo-SDHA with covalently attached FAD. His_6-SDHA was incubated with purified SDHAF2 and SDHAF4 as indicated and associated proteins were evaluated by SDS-PAGE. FAD was added at 75 µM and fumarate was added at 5 mM. Yellowish FAD fluorescence is observed when SDHA is covalently attached to FAD. ImageJ densitometry, shown at the bottom, was measured as arbitrary units (arb. units.) and used to evaluate the relative binding of SDHAF2 (teal) and SDHAF4 (brown) to SDHA. The y-axis on the densitometry quantitation expresses these as a ratio. a Input protein and pairwise interaction between SDHA and SDHAF2. (left) input SDHA, (right) interaction between SDHA and SDHAF2 in the presence of FAD and fumarate. Note that only after the addition of fumarate does the covalent bond between FAD and SDHA form (lane 3). b Pairwise interaction of SDHA and SDHAF4. c Interaction of SDHA with the assembly factors after incubation with both SDHAF2 and SDHAF4. d Displacement of SDHAF2 after purified holo-SDHA/SDHAF2 complex (2 µM) was incubated with SDHAF4. All Coomassie gels are representative of *n* = 4 independent experiments, bar graphs show mean values ± SD, and statistics were done by paired two-tailed Student's *t*-test. Source data are provided as a Source Data file.

(hPheo1[36]) and we re-expressed SDHAF4 in SDHAF4^{KO36} cells (SDHAF4^{rec}; see Supplementary Fig. 2a–h for characterization of the cell lines). We then evaluated whether SDHA could be assembled into CII using native blue gel electrophoresis followed by western blotting (Fig. 3).

For the parental hPheo1 cells, the vast majority of SDHA assembles into CII as expected (Fig. 3a, lane 1). In the SDHAF4^{KO} cells, only a small portion of the ~72 kDa SDHA assembles into CII, while the majority now comigrates with the ~18 kDa SDHAF2 at a molecular mass of ~100 kDa (Fig. 3a, lane 2). Re-expression of SDHAF4 allowed the majority of SDHA to again assemble into CII (Fig. 3a, lane 3). Notably, SDHAF4^{rec} cells had a > 10-fold increase in SDHAF4 as compared to the parental cell lines (Supplementary Fig. 2a, c) and also showed the presence of additional distinctly migrating bands that contained SDHAF4 (Fig. 3).

Given that SDHA and each of its assembly factors can comigrate at a molecular weight consistent with a complex and that these form robust direct interactions in purified proteins, one interpretation is that these proteins may be bound to each other in cells. As one step to propose the identity of the molecular species within these bands, we prepared some of the possible complexes from purified proteins, separated these on native and SDS gels, and compared the migration to the species that accumulate in cells (Supplementary Fig. 3a, b). This analysis is consistent with the assignment of SDHA-AF2 as the ~100 kDa species that accumulates in the SDHAF4^{KO} cells. Although SDHA-AF4 migrates at a higher molecular weight, it is not possible to definitively assign this as the ~150 kDa species that accumulates in the SDHAF4^{rec} cells (Fig. 3, lanes 2 and 3, Supplementary Fig. 2a) because other proteins could be part of the accumulating complex in cells. The remaining SDHAF4-containing bands in the SDHAF4^{rec} cells resemble the laddering observed when purified SDHAF4 is separated on native gels (Supplementary Fig. 3b) consistent with these being self-oligomers. To further interrogate the ~150 kDa band, we performed an immunoprecipitation analysis of the various cell lines following transfection with FLAG-SDHA (Fig. 3b). SDHA and SDHAF4 were both present in these cell lines, but we only observe robust immunoprecipitation of SDHAF4 with SDHA in the SDHAF4^{rec} cell line, which contains the ~150 kDa band.

Although the above studies suggest that these complexes form sequentially, they do not preclude a mechanism where SDHA-AF2 and SDHA-AF4 sub-assemblies form in parallel. To test this, we knocked out SDHAF2 from the SDHAF4^{KO36} cells. In these SDHAF2^{KO}/SDHAF4^{KO} cells, SDHA migrated at ~100 kDa (Fig. 3a, lane 4). We no longer detected the SDHA-AF4 species in the SDHAF2^{KO}/SDHAF4^{rec} cells, even though these cells contained >10-fold SDHAF4 (Fig. 3a, lane 5). Instead, we observed the laddering that hallmarks the self-oligomerization of SDHAF4 (Fig. 3a, panel 4, lane 5, Supplementary Fig. 3b). This result is consistent with: (1) the in vitro studies, which showed little interaction between purified SDHA and purified SDHAF4 (Fig. 2b); (2) a robust interaction between the pre-formed SDHA-AF2 complex and SDHAF4 (Fig. 2d); and (3) the immunoprecipitation (Fig. 3b), which showed that the SDHA-AF4 complex only coprecipitated when SDHAF2 was present. Taken together, the results suggest a strong preference for the SDHA-AF2 complex to form first under normal cellular conditions and little binding of SDHAF4 to SDHA in the absence of SDHAF2.

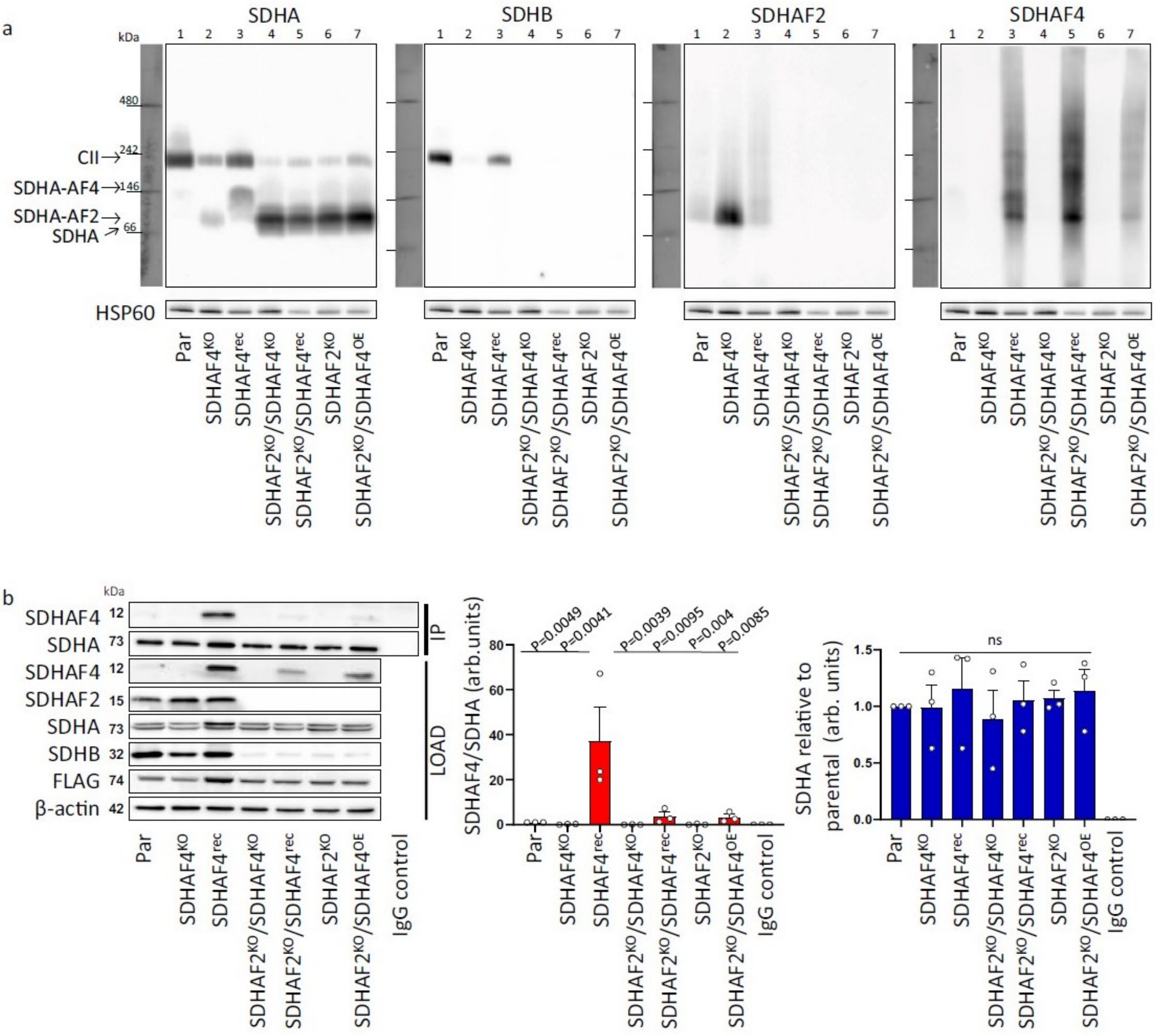

Fig. 3 | The complexes that accumulate upon perturbation of SDHAF2 and SDHAF4 levels in cells. a Mitochondria isolated from parental, SDHAF4^{KO36}, SDHAF4^{rec}, SDHAF2^{KO}/SDHAF4^{KO}, and SDHAF2^{KO}/SDHAF4^{rec} cells were subjected to native blue gel electrophoresis followed by western blotting using anti-SDHA, anti-SDHB, anti-SDHAF2, and anti-SDHAF4 IgG. HSP60 was used as a loading control, as assessed by anti-HSP60 IgG. Positions of CII and bands positive for SDHA, SDHAF2, or SDHAF4 are indicated, with most likely possibilities for the molecular complex indicated on the left. Western blots are representative of $n = 4$ independent experiments. For SDHAF4^{KO} cell lines, the quantity of CII subunits and assembly factors were generally as expected (Supplementary Fig. 2b, c); notably, the SDHAF4^{rec} cells exhibited a >10-fold increase in SDHAF4 levels as compared to the parental hPheo1 cells. SDHAF4^{KO} cells also showed the expected changes in routine respiration, CII-dependent respiration, CII-dependent succinate-converting activities, and succinate-fumarate ratio (Supplementary Fig. 2d–h). b Parental, SDHAF4^{KO36}, SDHAF4^{rec}, SDHAF2^{KO}/SDHAF4^{KO}, SDHAF2^{KO}/SDHAF4^{rec}, SDHAF2^{KO}, and SDHAF2^{KO}/SDHAF4^{OE} cells were transduced for stable expression of SDHA-FLAG. Lysates from all cell lines were then subjected to immunoprecipitation using anti-FLAG IgG and analyzed by western blotting for identification of SDHAF4 binding to SDHA. Results are representative of $n = 3$ independent IP experiments from 3 separate biological replicates ± SEM. ImageJ quantitation of each species is expressed as arbitrary units (arb. units). Statistics were done using GraphPad Prism8, 2-way ANOVA, and Tukey´s multiple comparison test, with individual variances computed for each comparison. Statistical differences for the SDHAF4/SDHA values are indicated by the symbol p values (Par vs. SDHAF4^{rec}, $p = 0.0049$; SDHAF4^{KO} vs. SDHAF4^{rec}, $p = 0.0041$; SDHAF4^{rec} vs. SDHAF2^{KO}/SDHAF4^{KO}, $p = 0.0039$; SDHAF4^{rec} vs. SDHAF2^{KO}/SDHAF4^{rec}, $p = 0.0095$; SDHAF4^{rec} vs. SDHAF2^{KO}, $p = 0.004$; SDHAF4^{rec} vs. SDHAF2^{KO}/SDHAF4^{OE}, $p = 0.0085$). No statistical significance (ns) was found between cell lines for data on SDHA level relative to parental cells (p values are 0.0 to 0.99). Source data are provided as a Source Data file.

SDHA-AF2-AF4 is the second protein-protein complex formed during SDHA maturation

In the SDHA-AF2 complex, SDHAF2 interacts with SDHA at the same surface where SDHB would bind to SDHA in the assembled CII[32]. Thus, SDHAF2 must be removed from SDHA for CII to assemble. However, displacing SDHFA2 during maturation may be non-trivial. The purified SDHA-AF2 complex is highly stable and requires denaturants for it to disassociate in vitro[37]. To better understand how SDHAF4 displaces SDHAF2 from SDHA, we used a structural approach. We first sought to capture early intermediates in the process. To do this, we identified that temperature could affect the kinetics of SDHAF2 displacement from SDHA, with lower temperatures slowing the process. As a result, mixing SDHA-AF2 with SDHAF4 at 4 °C slows SDHAF2 displacement and results in the capture of an SDHA-AF2-AF4 intermediate.

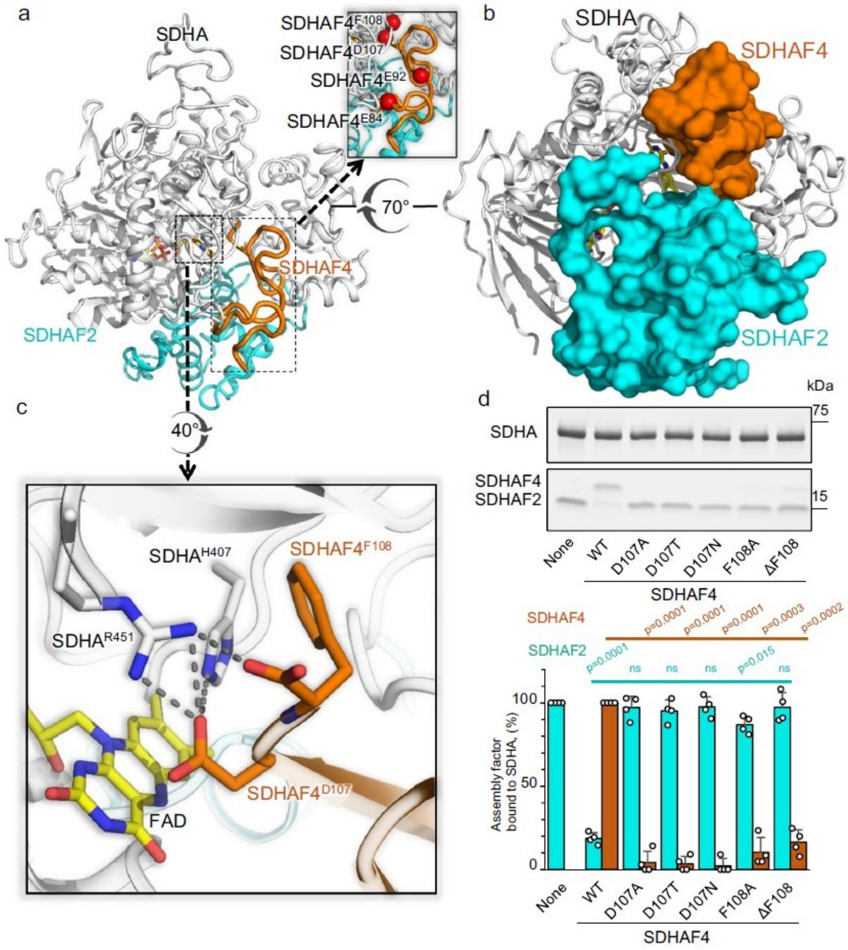

Fig. 4 | Structure of the SDHA-AF2-AF4 complex. a Ribbon diagram of the human SDHA-AF2-AF4 complex. SDHA is shown in gray, SDHAF2 is shown in cyan, and SDHAF4 is shown in orange. The covalent FAD is shown as a stick representation with carbons yellow, oxygens red, nitrogens blue, and phosphorous orange. The isoalloxazine functional group of the FAD is positioned between the flavin-binding domain of SDHA and the C-terminus of SDHAF4. Key interactions are shown in the inset. b Orientation of SDHAF2 and SDHAF4 in the complex. SDHA is shown as ribbons and SDHAF2 and SDHAF4 are shown as space-filling. The view is rotated 70° around the x-axis as compared to the view in (a). c Interactions between the C-terminus of SDHAF4 and the SDHA active site. The position of the conserved C-terminus is stabilized by interactions between $SDHAF4^{D107}$ and $SDHAF4^{F108}$ and SDHA active site residues $SDHA^{R451}$ and $SDHA^{H407}$. d Validation of SDHAF4 binding residues using mutagenesis. SDHAF4 containing the indicated C-terminal mutations was evaluated for the ability to displace SDHAF2 from the SDHA-AF2 complex. The assembly factors that remained bound to SDHA were visualized after the separation of the reaction on an SDS-PAGE gel. Mutations involved $SDHAF4^{D107}$ ($SDHAF4^{D107A}$, $SDHAF4^{D107T}$ and $SDHAF4^{D107N}$), and $SDHAF4^{F108}$ ($SDHAF4^{F108A}$ and $SDHAF4^{\Delta F108}$). The SDS-PAGE gel is representative of $n = 4$ independent experiments. ImageJ quantitation of SDHAF2 (teal) and SDHAF4 (brown) was used to calculate the percentage of each assembly bound to SDHA, as compared to a control (100%). This is expressed on the y-axis of each bar graph as mean values ± SD. Bar graphs show mean values ± SD, and statistics were calculated by paired two-tailed Student's t-test. Source data are provided as a Source Data file.

Supporting this intermediate as relevant to SDHAF2 displacement, incubating the SDHA-AF2-AF4 at 25 °C overnight or 37 °C for 4–5h allowed for the spontaneous release of SDHAF2.

We purified the metastable species that formed from a mixture of SDHA-AF2 and SDHAF4 at 4 °C, crystallized the species, and determined the structure by X-ray crystallography (Supplementary Table 1, Fig. 4). This identified an SDHA-AF2-AF4 assembly intermediate (Fig. 4a). Here, SDHAF2 and SDHAF4 bind adjacent to each other on the surface of SDHA (Fig. 4b). Despite adjacent binding, each of these assembly factors interacts with SDHA, but not with each other (Supplementary Table 2).

As relates to the control of maturation, the most striking aspect of the SDHA-AF2-AF4 structure is the decrease in the intrinsic disorder of both assembly factors. In terms of SDHAF2, the N- and C-termini were fully disordered in the NMR structure of the isolated yeast SDHAF2 homolog[38] and were partially disordered in the crystal structure of the SDHA-AF2 complex[32] (Supplementary Fig. 4a, b). In the SDHA-AF2-AF4 structure, both the N- and C-termini of SDHAF2 strongly interact with SDHA (Supplementary Fig. 4c, d, Supplementary Table 2), but the additional ordering does not involve a significant increase in secondary structure. Outside of the increased ordering of the termini, the fold of SDHAF2 largely resembles that described previously[32] except for a shift of amino acids $SDHAF2^{146\text{-}153}$ by 4.5 Å (Supplementary Fig. 4d).

Perhaps more intriguing is the structural organization of SDHAF4. Here, we used both circular dichroism (CD) spectroscopy (Supplementary Fig. 5a, b) followed by NMR-based backbone assignments of chromatographically pure protein (Supplementary Fig. 5c–f,

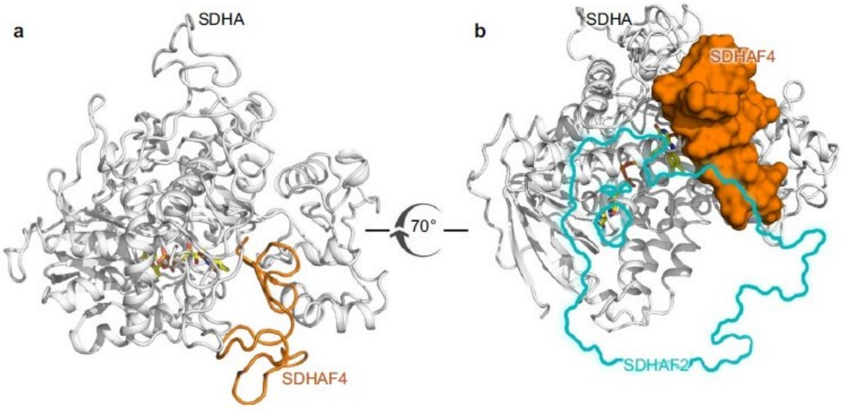

Fig. 5 | Structure of the SDHA-AF4 complex. a The SDHA-AF4 structure is shown as a ribbon representation with SDHA shown in gray and SDHAF4 shown in orange. Covalently bound FAD is shown in stick representation (b) A rotated view of the SDHA-AF4 structure with SDHAF4 shown as space-filling. The location of SDHAF2 from the SDHA-AF2-AF4 structure is shown as a cyan outline. Overlap between the binding sites for SDHAF2 and SDHAF4 suggests that the ordering of SDHAF4 could help to displace SDHAF2.

Supplementary Table 3) to show that isolated SDHAF4 is a disordered protein (Supplementary Fig. 5g, h). However, when in complex with SDHA, the C-terminal 34 residues of SDHAF4 are associated with clear electron density (Supplementary Fig. 6a). The ordered region of the protein, comprising SDHAF4$^{75-108}$, has little secondary structure and contains only two short β-strands (Supplementary Fig. 6a, b). Extensive interactions between SDHAF4 and SDHA (Supplementary Table 2) involve strongly conserved residues from both proteins and hinge upon intimate contacts between the two C-terminal residues of SDHAF4 (SDHAF4^{D107} and SDHAF4^{F108}) and the active site SDHA^{H407} and SDHA^{R451} of SDHA (Fig. 4c).

Curiously, SDHAF4^{D107} and SDHAF4^{F108} at the C-terminus of SDHAF4 form tight interactions at the active site, with SDHAF4^{D107} acting as a dicarboxylate mimetic. To do this, SDHAF4^{D107} makes strong interactions with the active site residues that normally bind dicarboxylate: SDHA^{H407} and SDHA^{R451} (Fig. 4c). Moreover, the C-terminal SDHAF4^{F108} occludes the location that would be occupied by the dicarboxylate substrate in assembled CII. Taken together, these two C-terminal residues of SDHAF4 contribute to the strong SDHAF4 binding to SDHA. In addition, these residues almost certainly preclude the binding of substrates or inhibitors to the SDHA subunit during the CII assembly process. These interactions also prevent solvent exposure of the FAD during assembly, which could prevent catalysis and impede the formation of reactive oxygen species.

Supporting the C-terminus of SDHAF4 as important for function, residues equivalent to SDHAF4^{D107} and SDHAF4^{F108} are strictly conserved in all SDHAF4 homologs, including putative homologs from a variety of α- and γ-proteobacteria (Supplementary Fig. 6c). To validate the importance of this interaction, we prepared five mutations of the C-terminus (Fig. 4a (*inset*)) and assessed the impact on binding and disassociation of the holo-SDHA-AF2 complex. All five variants showed reduced, albeit detectable, binding to SDHA-AF2 (Fig. 4d, Supplementary Fig. 7a–g) but were unable to disassociate the SDHA-AF2 complex (Fig. 4d).

Synthesis of the structural and biochemical data also suggests how SDHAF4 interacts with the SDHA-AF2 complex. The SDHA-AF2-AF4 structure suggests that dicarboxylate bound at the active site would compete for the binding of SDHAF4 to SDHA since SDHAF4^{D107} binds at the same location and engages some of the same amino acid residues as the dicarboxylate. Our in vitro experiments (Fig. 2d), however, show that fumarate does not compete with SDHAF4 for binding to SDHA. This suggests that SDHAF4 may initiate attachment to SDHA at a site distant from the active site. Other notable residues of SDHAF4 that could initiate contact with SDHA-AF2 involve the conserved SDHAF4^{E84} and SDHAF4^{E92}, which interact with the conserved SDHA^{R171} (Fig. 4a (inset), Supplementary Fig. 7h). We again used mutagenesis to assess how these conserved residues affected the binding and disassociation of the holo-SDHA-AF2 complex (Fig. 4a (inset), Supplementary Fig. 7h–j). Here, SDHAF4^{E92N} still binds to SDHA-AF2 but displaces only ~40–50% of SDHAF2 (Supplementary Fig. 7k). However, SDHAF4^{E84N} did not detectably bind to the SDHA-AF2 complex (Supplementary Fig. 7k). This may suggest that the initial attachment of SDHAF4 to SDHA is through these residues more distant from the conserved SDHAF4 C-terminus. Binding would restrict the movement of the capping domain and would allow the C-terminus of SDHAF4 to fold into the location seen in the SDHA-AF2-AF4 structure.

SDHA-AF4 is the third protein-protein complex in SDHA maturation

As the studies in cells suggest that the next metastable intermediate in the biogenesis of CII likely involves the removal of SDHAF2 from SDHA (Fig. 3, lane 3), and the studies in vitro identify that SDHAF4 can displace SDHAF2 (Fig. 2d), we hypothesized that an SDHA-AF4 complex would be the next intermediate and sought to capture this complex. To do this, we added an excess of SDHAF4 to SDHA-AF2, incubated this mixture at room temperature overnight, purified the resultant SDHA- and SDHAF4-containing species, and determined the crystal structure (Supplementary Table 1). In the SDHA-AF4 complex (Fig. 5a, b, Supplementary Table 4), nine additional amino acids of SDHAF4 are ordered as compared to SDHA-AF2-AF4, such that residues 66–108 are now associated with clear electron density (Supplementary Fig. 8a, b). Although this is accompanied by a small increase in the number of interactions between SDHA and SDHAF4 (Supplementary Table 4) most of the direct interactions appear similar to those observed in the SDHA-AF2-AF4 complex, including the intimate interactions between the SDHAF4 C-terminus and the SDHA active site (Fig. 4c, Supplementary Fig. 8c). Importantly, this newly ordered region could affect other binding partners in multiple ways. First, it would sterically conflict with the binding position of SDHAF2 that is observed in both the SDHA-AF2 and SDHA-AF2-AF4 complexes (Fig. 5b, Supplementary Fig. 8d) and with the binding position for SDHB in assembled CII (Supplementary Fig. 9). In addition, the changes in disorder of SDHAF2 and SDHAF4 allosterically affect the angle between two domains of SDHA (Supplementary Fig. 10), which modifies this same binding surface (Supplementary Fig. 9). This suggests that the change in the disorder of the assembly factors accompanies the transfer of SDHA from one binding partner to the next.

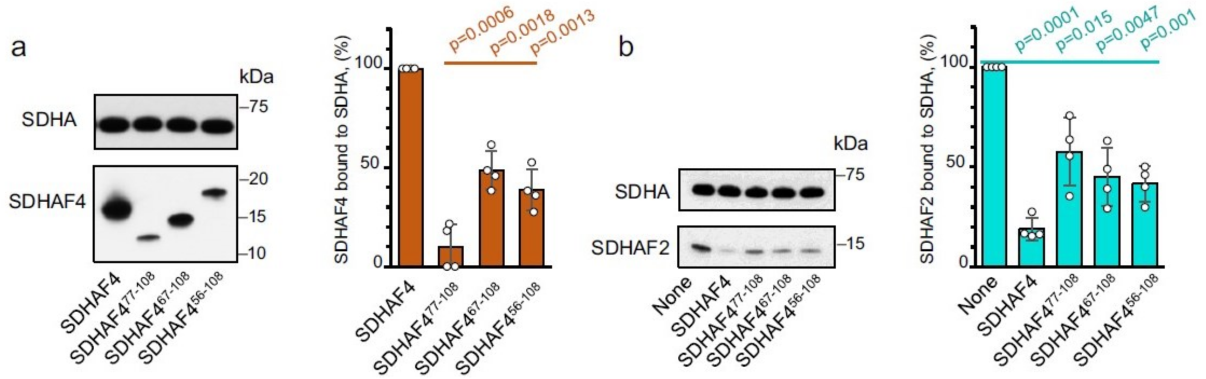

Fig. 6 | Intrinsically disordered regions of the SDHAF4 sequence support binding to the SDHA-AF2 complex. a Three N-terminal truncated versions of SDHAF4 (SDHAF4$^{77-108}$, SDHAF4$^{67-108}$, and SDHAF4$^{56-108}$) were designed based on prior structural[32] and cellular[28] studies and assessed for binding to SDHA-AF2. Full-length SDHAF4 (left lane) bound strongly, while each truncation variant bound at lower levels. ImageJ quantitation of SDHAF4 (brown) bound to SDHA for each mutant was measured and normalized to the amount of wild-type SDHAF4 that binds to SDHA under the same conditions. This is shown on the bar graph, with the *y*-axis indicating the normalized binding of SDHAF4 as a percent. b Regions of the protein that are intrinsically disordered facilitate SDHAF2 displacement. Each of the three SDHAF4 truncations was assessed for the ability to displace SDHAF2 from the SDHA-AF2 complex. The bar graph shows ImageJ quantitation of SDHAF2 (teal) normalized to the amount of wild-type SDHAF2 bound to SDHA, with the *y*-axis showing this as a percent. The SDS-PAGE gels in both (a) and (b) are representative of $n = 4$ independent experiments. ImageJ quantitation of each species was used to calculate the percentage bound, as expressed on the *y*-axis of each bar graph as mean values ± SD. Statistics were calculated by paired two-tailed Student's *t*-test. Source data are provided as a Source Data file.

Intrinsic disorder of the assembly factors is required to transfer SDHA between complexes

To test whether the regions of intrinsic disorder are important for the transfer of SDHA from SDHA-AF2 to SDHA-AF4, we developed variants that removed different amounts of the disordered N-terminus of SDHAF4 and tested these for binding to SDHA-AF2 (Fig. 6a) and displacement of SDHAF2 from that complex (Fig. 6b). Of these, SDHAF4$^{77-108}$ contains only the amino acid residues that are structured in the SDHA-AF2-AF4 crystal structure. SDHAF4$^{67-108}$ and SDHAF4$^{56-108}$ contain all residues that are ordered in both crystal structures. The deleted regions of these latter two variants have no detectable sequence similarity across known SDHAF4 homologs (Supplementary Fig. 6c), further supporting that we are only eliminating regions that are always disordered.

Full-length SDHAF4 displaced ~80% of SDHAF2 from the SDHA-AF2 complex (Figs. 2d and 6b). In comparison, each of the truncations was impaired in the ability to bind to the SDHA-AF2 complex (Fig. 6a) and to disassociate this complex (Fig. 6b). The shorter constructs each removed only ~50% of SDHAF2 from SDHAF4 (Fig. 6b) despite the presence of all residues observed in the crystal structures (Fig. 5). These findings implicate the intrinsically disordered regions in the process of replacing SDHAF2 with SDHAF4 during SDHA maturation.

Discussion

CII activity connects the Krebs cycle[39] with bioenergetics during aerobic respiration, oxygen limitation[40], or sulfide signaling[41]. This activity makes CII a master controller of metabolism. CII activity also affects succinate signaling, which has broad implications for cells. One way to regulate CII-dependent succinate oxidation is via its assembly. A critical aspect of the assembly process is the maturation and handling of the catalytic SDHA subunit.

We show that during the preferred pathway of maturation, SDHA proceeds through at least three metastable intermediates (Fig. 7): SDHA-AF2[32] (Fig. 3a, lane 2), SDHA-AF2-AF4 (Fig. 4a, b), and SDHA-AF4 (Fig. 3a, lane 3, Fig. 5a). Of these, both SDHA and SDHA-AF2 migrate as a ~100 kDa band on native PAGE. Past reports identify that there is a specific increase in the ~100 kDa species under a variety of physiological conditions. The earliest reports identified that SDHA migrated as a ~100 kDa species following mitochondrial acidification[23]. At the time, this was interpreted as an SDHA-SDHB heterodimer[23], and the concept of dynamic disintegration of CII into an SDHAB heterodimer has been retained in the literature. However, this ~100 kDa species was not evaluated for the presence of SDHB. Similar ~100 kDa assemblies containing SDHA were noted in cells where the assembly of CII was disrupted, and these were termed CII$_{low}$[20]. Mass spectrometry of a band excised from native gels detected SDHA, SDHAF2, and SDHAF4[20], although the abundance of each of these components and the nature of the underlying molecular species that formed this band was not clear at that time. Most recently, macrophage activation was shown to be associated with CII disassembly and with the appearance of a ~100 kDa species containing SDHA but not SDHB[21]. This band was not probed for the presence of assembly factors and its components beyond SDHA were not suggested. Taken together, the precise molecular composition of the ~100 kD band that accumulates under a variety of biological and pathological conditions has been elusive.

SDHAF4 knock-out cells show the accumulation of a ~100 kDa band, which may indicate that dynamic disassembly and assembly are reversible processes of each other. To determine the molecular nature of the ~100 kDa species, we combine six observations. First, western analysis of the ~100 kDa species shows that this almost exclusively contains SDHA and SDHAF2. Second, purified SDHA-AF2 migrates in a band centered at ~100 kDa (Fig. 3, Supplementary Fig. 3). Third, SDHA-AF2 is highly stable, and the purified protein does not disassociate in the absence of denaturation. Fourth, purified SDHAF4 forms oligomers, with one of these coincidentally migrating at ~100 kDa (Supplementary Fig. 3). Fifth, SDHAF4 is not consistently detected in the ~100 kDa band[20]. Sixth, both SDHA-AF2-AF4 and SDHA-AF4 migrate distinctly in bands centered at ~150 kDa (Supplementary Fig. 3, Fig. 3). We therefore propose that the molecular species that most increases in abundance under pathological conditions as a ~100 kDa band is likely the SDHA-AF2 assembly intermediate and that the inconsistent observation of SDHAF4 is due to comigration of the SDHAF4 oligomers that form under some cellular conditions. We cannot exclude the fact that isolated SDHA or other SDHA-containing assemblies are also present under some pathological conditions.

We further find that SDHAF4 allows SDHAF2 to be released from the SDHA-AF2 complex and that changes in intrinsic disorder may be important for allowing this to proceed. Mechanistically, these changes in disorder induce allosteric structural changes in SDHA

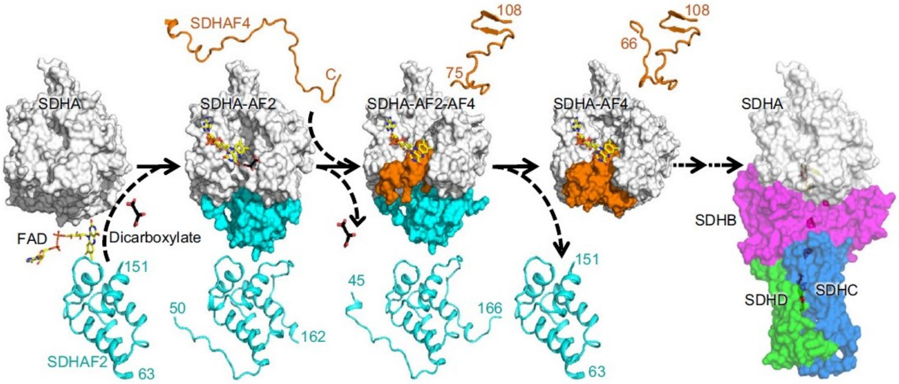

Fig. 7 | Model for the preferred maturation pathway of SDHA. Synthesis of the data suggests a preferred pathway for SDHA maturation in healthy cells. The compositions of SDHA-containing assembly intermediates that are formed during the CII biogenesis are shown as space-filling models in the center. Both the FAD and the dicarboxylate are shown superposed above each structure to help illustrate the maturation process, but these molecules are buried and shielded from solvent in the SDHA-AF2-AF4 and SDHA-AF4 structures. A ribbon diagram of SDHAF2 in each structure is shown at the bottom, and a diagram of SDHAF4 in each structure is shown at the top. In the first step, apo-SDHA binds FAD, dicarboxylate, and SDHAF2 to form the first metastable intermediate. In this process, the disordered termini of isolated SDHAF2 partially organize along the surface of SDHA but do not form secondary structure. This metastable SDHA-AF2 uses bound dicarboxylate as a cofactor to promote the covalent attachment of FAD, and form holo-SDHA-AF2. In the second step, SDHAF4 binds to form SDHA-AF2-AF4. Here, both termini of SDHAF2 further increase their organization. In addition, the C-terminal region of SDHAF4 becomes organized but has little secondary structure. Notably, the C-terminus of SDHAF4 occludes the dicarboxylate binding site, and dicarboxylate is released. In the third step, the additional organization of SDHAF4 displaces SDHAF2 and forms SDHA-AF4. The active site dicarboxylate-binding position remains occluded in this structure, although we note that the dicarboxylate malonate binds at a distal position in the structure. This distal site is of unknown relevance to the CII maturation process. Whether SHAF4 binds to another protein prior to or during its interaction with SDHA in cells remains unknown at this time. In addition, the handling steps of SDHA following this initial maturation process but prior to integration into functional CII (PDB ID 3SFD)[76] remains unknown at this time.

(Supplementary Fig. 10) that affect the binding surface that sequentially interacts with SDHAF2, SDHAF4, and SDHB (Fig. 7, Supplementary Fig. 9). In SDHAF2, the change in intrinsic disorder is found at the extremes of both the N- and C-termini (Supplementary Fig. 4a, b), and these regions are critical for SDHA maturation[32]. For SDHAF4, the isolated protein is fully disordered and a large segment at the N-terminus remains disordered even after binding to SDHA (Supplementary Figs. 5, 6a, b, 8a, b). The use of protein disorder to select binding partners in a temporal order may allow the system to remain dynamic. A role in protein assembly adds to the known functions of protein disorder.

Evaluation of deposited PDB coordinates identifies that changes in protein disorder accompany the biogenesis of many types of macromolecular complexes. These complexes range from small homomeric oligomers to large heteromeric complexes, include stable and transient complexes, proteins from all kingdoms, and proteins that localize in different compartments of the cell. Moreover, the changes in disorder can involve either assembly factors or the assembling protein.

Changes in disorder in assembly factors appear to be common, as exemplified by the assembly chaperone pICln (PDB entries 4F7U[42] and 1ZYI[43]) (Supplementary Fig. 11a–c) and the Cox17 and Sco1 assembly factors (PDB entries 1U96, 1U97, 2GT5, 2GQK and 2GQM) (Supplementary Fig. 11d–g)[44,45]. Changes in disorder are also observed in self-assembling complexes, as exemplified in many of the transient complexes of mammalian signal transduction. Notable exemplars are the mammalian arrestins, which can be found as monomers (PDB entry 3P2D[46]), as isoform-specific trimers (PDB entry 5TV1[47]), or in complex with each of >800 receptors[48,49]. Arrestins contain a loop that undergoes dynamic transitions during this process and can be disordered or ordered with different secondary structures, allowing the necessary plasticity to assemble into multiple types of distinct complexes (Supplementary Fig. 12a–c). A second example of changes in disorder regulating self-assembly is found in the bacteriophage nuclear shell[50,51]. Dynamics and disorder were observed at the N- and C-termini of the chimallin protein of this nuclear shell (Supplementary Fig. 13a, b) (PDB entry 7SQU[52].

A common theme of changes in disorder during assembly is that newly ordered regions tend to lack substantial secondary structure. The paucity of secondary structure is observed in the newly ordered regions of SDHAF2, SDHAF4, arrestin[48,49], and chimallin[52] but is perhaps best exemplified in mammalian mitochondrial complex I (PDB entry 5XTD[53]) (Supplementary Fig. 14a). NDUFS4 and NDUFS6 are assembly factors that double as accessory subunits for complex I. Solution structures of isolated bacterial homologs of NDUFS4 and NDUSF6 (PDB entry 2JYA[54] and 2JRR[55]) show compact folds with disordered termini (Supplementary Fig. 14b–h). However, when bound as accessory subunits, these assembly factors have significant regions without secondary structure[56], which is accompanied by a change in the architecture of the folded regions (Supplementary Fig. 14b–h). Because secondary structure imparts stability, it is tempting to speculate that the low levels of secondary structure reflect a need for structural plasticity during the assembly process. This could help to support dynamic switching between binding partners.

Together, our findings here describe previously unknown steps of CII biogenesis. Our results indicate that intrinsic disorder in the assembly factors is important for sequential transition of SDHA subunit between metastable assembly intermediates. This ensures that the final complex contains fully mature SDHA and reduces the incorporation of a partially functional subunit, for example, SDHA with non-covalent FAD. Evaluation of assembly snapshots for unrelated structures suggests that changes in intrinsic disorder may be common during the process of assembly in a range of types of biological complexes. The ordering of these disordered regions correlates with regions of proteins that have unusually little secondary structure, which may further increase plasticity and allow the dynamic exchange of binding partners.

Methods

Plasmids

Plasmids pQE-hSDHA (non-cleavable N-terminal His-tag), pQT-SDHAF2 (TEV-cleavable His tag), and pQE-hSDHA-37-SDHAF2 for co-expression of His_6-SDHA and untagged SDHAF2 were used[32,37]. The original pQE-hSDHA-37-SDHAF2 was constructed to produce a single polycistronic transcript that included His6-SDHA under the T5 promoter and untagged mature 37SDHAF2 (residues 37–166) that retained the Shine-Delgarno translational enhancer from the original pQE80L plasmid. For expression of SDHAF2 with a TEV cleavable 6xHis N-terminal tag, the BamHI- HindIII fragment encoding amino acid residues 37–166 of SDHAF2 was cloned into pST50Trc1-HISNDHFR (Addgene[57]). The DNA sequence encoding the mature SDHAF4 protein (amino acid residues 20–108) was optimized for *E. coli* expression, synthesized (Genscript), and cloned into the 5′ BamHI and 3′KpnI fragment of pST50Trc3-FLAG (Addgene[57]). The His$_6$-SDHAF4 plasmid was constructed using the BamHI-SalI fragment encoding amino acid residues 30–108 of SDHAF4, which was cloned into the pQT vector[37] to create pQT-SDHAF4. N-terminally truncated SDHAF4 variants were fused with the maltose binding protein (MBP) using the pMAL vector (Addgene[57]). The plasmids encoding the SDHAF4 variants (SDHAF4^{D107A}, SDHAF4^{D107N}, SDHAF4^{D107T}, SDHAF4^{F108A}, and SDHAF4$^{\Delta F108}$) were created by modification of the pQT-SDHAF4 parent vector (Genscript). All plasmids developed for protein expression in *E. coli* lacked the mitochondrial targeting sequence.

Protein expression and purification for biochemical and structural studies

Proteins for both biochemical and structural studies were expressed in *E. coli* BL21(*DE3*). Bacteria transformed with the appropriate plasmid were grown to OD$_{600}$ = 0.5 and protein expression was induced with 0.1 M IPTG (Fisher Scientific, Cat No. NC1105120) followed by growth for 17 h at either 17 °C or 20 °C. Cells were harvested by centrifugation and then stored at −70 °C until used.

For FLAG-SDHAF4, *E. coli* cells were suspended in 20 mM HEPES pH 7.5 supplemented with protein inhibitor cocktail (Roche, 11873580001), sonicated, and centrifuged at 100,000 g for 1 h. The clarified lysate was then loaded onto a DEAE-Sepharose column equilibrated with 20 mM HEPES pH 7.5 and the FLAG-SDHAF4 protein was eluted with 20 mM NaCl in the same buffer. This fraction was filtered through 30 kDa Amicon filters (Millipore Sigma, UFC903008), concentrated on 10 kDa Amicon (Millipore Sigma, UFC903008) filtration units and washed by diluting the concentrated protein 20 times with 20 mM HEPES pH 7.5, 10% glycerol, 1 mM DTT and concentration with a 10 kDa Amicon (Millipore Sigma, UFC903008) filtration unit.

Truncated SDHAF4 variants were expressed as His$_6$-MBP-FLAG fusions and purified using Ni^{2+}-affinity chromatography. Isolated fusion proteins were treated with TEV protease to cleave MBP in 50 mM Tris, pH 7.5, 0.5 mM EDTA, and 1 mM DTT for 17 h at 7 °C. The proteolytic reactions were applied to a Ni-NTA column and the flow-through fractions containing FLAG-SDHAF4 were concentrated with 3 kDa Amicon (Millipore Sigma, UFC900396) filtration unit.

Human SDHA-AF2 complex was purified using Ni^{2+} affinity (HisTrap HP, Millipore Sigma, GE17-5248-01) followed by anion exchange (HiTrap DEAE Sepharose FF, Cytiva, 1751540). Final purification was done using size exclusion chromatography (Superdex S200 increase, Cytiva, 28990944) in 20 mM HEPES pH 7.5 buffer[32]. Apo-SDHA was expressed and purified as described above, except that the final size exclusion chromatography step was omitted. For binding assays, His$_6$-SDHAF2 was treated with TEV protease to remove the His$_6$-tag as described above[32].

SDHA binding to SDHAF4 and SDHAF2

The interactions between SDHA and the SDHAF2 and SDHAF4 assembly factors were evaluated by a pull-down approach. His$_6$-apo-SDHA (2.6 μM) was incubated with SDHAF2 (6.4 μM), FLAG-SDHAF4 (8 μM) or both assembly factors in 40 mM HEPES, pH 7.5, 0.5 mM DTT for 30 min at 25 °C. FAD (75 μM) and/or 5 mM fumarate were added as indicated. Ni-NTA agarose resin (30 μl) was added and after an additional 10 min incubation, the resin was washed 3 times with 1.3 ml of 20 mM potassium phosphate, pH 7.5, 0.1 M NaCl, 0.5 mM DTT, and 25 mM imidazole. His$_6$-SDHA and any bound proteins were eluted with 2x SDS loading buffer (BioRad, 1610737) and separated by SDS-PAGE on "AnykD™" pre-cast protein gels (BioRad, 4568023). The gel was stained with InstantBlue Coomassie stain (Abcam, 50-196-3787) and analyzed by ImageJ (NIH).

To test the effect of SDHAF4 and fumarate on the stability of the holo-SDHA-AF2 complex, apo-SDHA (2.6 μM) was incubated with SDHAF2 (3.2 μM), 20 μM FAD, and 0.25 mM fumarate for 30 min at 25 °C. This results in the formation of holo-SDHA-SDHAF2 complex. To remove unbound components, the reaction mixture was concentrated on a 0.5 ml 50 kDa Amicon Ultra (Millipore Sigma, UFC905096) centrifugal filter unit and washed twice with 0.5 ml of 40 mM HEPES pH 7.5, 0.5 DTT. Holo-SDHA-SDHAF2 (2 μM) was next incubated with SDHAF4 in the presence or absence of 5 mM fumarate for 30 min at 25 °C and immobilized on Ni-NTA agarose beads, as described above. Note that FLAG-SDHAF4 (MW: 12.4 kDa) runs anomalously in the Tris/Glycine/SDS buffer at an apparent molecular weight of ~17 kDa. This forms a distinct band above SDHAF2 (MW: 15.6 kDa) allowing easy visualization in the Tris/Glycine/SDS buffer system. Because some truncated FLAG-SDHAF4 variants were similar in size to SDHAF2, the detection of SDHA, SDHAF2, and FLAG-SDHAF4 variants was done using western analysis with a Fast Western Kit, ECL substrate (Pierce, 35055), and the following primary antibodies: anti-FLAG, 1:1000 dilution (GenScript, A00187), anti-SDHAF2, 1:1000 dilution (SDH5, 45849, Cell Signaling Technology), anti-SDHA 1:2000 dilution (Cell Signaling Technology, 11998).

Evaluation of the association between FLAG-SDHAF4 and SDHAF2

Purified SDHAF2 (8 μM) and FLAG-SDHAF4 (4 μM), or SDHAF2 alone, were incubated in 40 mM HEPES, pH 7.5, 0.5 mM DTT, for 30 min at 25 °C and then with 10 μl ANTI-FLAG-M2 Affinity gel (Millipore Sigma, A2220-1ML) for another 15 min. The gel was washed with 20 mM potassium phosphate pH 7.5, 0.1 M NaCl, 0.5 mM DTT, 25 mM imidazole. The proteins were eluted with 2x SDS loading buffer (BioRad, 1610737) and separated by SDS-PAGE. After Coomassie staining, the bands corresponding to SDHAF4 and SDHAF2 were evaluated by densitometry (ImageJ).

Oligomerization of purified SDHAF4

To assess oligomerization of purified SDHAF4, His$_6$-SDHAF4$^{30\text{-}108}$ was purified using Ni-NTA followed by size-exclusion chromatography. The eluted samples were then concentrated to 5 mg/ml, a dilution series was made, and the samples were loaded onto 10% native and 10% SDS gels. Since the molecular weight marker, NativeMark™ (ThermoFisher Scientific, LC0725) runs anomalously, purified *E. coli* FrdA and human SDHA and the SDHA-AF2 complex were used as standards for native PAGE. The samples of the SDHA-AF2-AF4 and SDHA-AF4 complexes were prepared by dissolving their crystals in 20 mM HEPES PH 7.5.

CD spectroscopy

Far-UV CD measurements of His$_6$-tagged human SDHAF4 and SDHA-SDHAF2 were recorded at 4 °C, 15 °C, and 25 °C on a Jasco J-1500 Spectropolarimeter with Peltier control using 1-mm Quartz cuvettes (Jasco, Tokyo). Far-UV CD spectra for His-SDHAF4 were collected at 50 μM, 100 μM, and 150 μM concentrations while spectra for the His-SDHA-SDHAF2 complex were collected at a 50 μM concentration. The CD spectra were collected in buffer containing 20 mM KF, pH 7.5, 0.5 mM DTT. Wavelength was scanned from 240 to 185 nm for His$_6$-SDHAF4 and from 250 to 195 nm for the His$_6$-SDHA-SDHAF2 complex. The scan speed was 100 nm/min with 10 accumulations and a response time of 1 sec.

Perturbation of SDHAF4 levels in hPheo1 cell lines

For experiments in cells, a progenitor cell line previously derived from adrenal cells from a human pheochromocytoma tumor (hPheo1[36]), developed by Dr. Hans Ghayee, was maintained in RPMI medium (Sigma-Aldrich) supplemented with 10% fetal bovine serum, antibiotics, and pyruvate (1 mM), glucose (4.25 g/l) and uridine (50 mg/l) at 37 °C under 5% CO_2. Genomic deletion of the *SDHAF2* and *SDHAF4* genes was performed using the CRISPR/AsCas12a (also known as AsCpf1) system[58], chimeric Cas12a, and guide RNA-expression plasmid pX AsCpf1-Venus-NLS (gift from Dr. Björn Schuster, Institute of Molecular Genetics, Czech Academy of Sciences). Suitable crRNAs were identified using Crispor software (http://crispor.tefor.net/). Oligonucleotides were designed to provide the overhangs 5′-AGAT and 3′-TTTT (AAAA reverse complement) for cloning. Nucleotides contained an array of three crRNAs (SDHAF2^{KO} and SDHAF4^{KO36}) or one crRNA (SDHAF4^{KO81}). The crRNA sequences were separated by AsCas12a direct-repeat sequence (AAT TTC TAC TCT TGT AGA T). For *SDHAF2*, the critical exon 2 was targeted by frameshifting. The *SDHAF4* gene has no critical exons, so exon 2 was targeted either using 3 crRNAs (clone 81) or by introducing a frameshift using a single crRNA (clone 36). The oligonucleotides were cloned into a plasmid cleaved by FastDigest BpiI (Thermo Fisher Scientific, FERFD1014), and the correct insertion was confirmed by colony PCR and DNA sequencing (primers for SDHAF4^{forward}: CCA GGA AGG GAA ATG GCT GGA, SDHAF4^{reverse}: CTT TTC GTT GAG TTA TTG GAG TCC T; SDHAF2^{forward}: TTT CAG GGG GAT AGG GTC CG, SDHAF2^{reverse}: AAT TAC CCG GGT GTG GTG AC). hPheo1 cells were transfected with the verified AsCas12a constructs using Lipofectamine 3000 (Thermo Fisher Scientific, L3000008), followed by single-cell sorting for Venus-positive cells into a 96-well culture plate. Clones were collected, and deletion of the targeted locus was confirmed by genomic PCR and/or by Sanger sequencing. The SDHAF2^{KO}/SDHAF4^{KO} cell line was developed using the same procedure but starting with verified SDHAF4^{KO36} cells and knocking out SDHAF2.

To re-express SDHAF4 in SDHAF4^{KO} cell lines, the pCDH-SDHAF4 vector was prepared. To do this, SDHAF4 cDNA[28] (a gift from Jared Rutter, University of Utah) was sub-cloned into the pCDH-CMV-MCS-EF1 vector, which contains a neomycin (System Biosciences, CD514B-1) selection marker. SDHAF4 was amplified and appropriate restriction sites were added using iProof High-Fidelity DNA Polymerase (Biorad, 1725301). Sequences of primers are as follows: SDHAF4^{forward}: TAA GCA TCT AGA CCA CCA TGA CCC CAT CGA GGC TTCC, SDHAF4^{reverse}: TGC TTA GGA TCC TTA AAA ATC AAT ACA GCG TCC TTT TCG TTC. Target vector and PCR products were digested using FastDigest enzymes BamHI and Xba1 (Thermo Fisher Scientific, FD0054 and FD0684, respectively). The cleaved materials were separated on an agarose gel (Nippon Genetics, AG02), purified with Nucleospin Gel and PCR clean-up kit (Macherey-Nagel, 740609), and ligated into the vector using T4 DNA ligase (Thermo Fisher Scientific, 15224017). The ligation reaction was transformed into One Shot Stbl3 chemically competent *E. coli* (Invitrogen, C737303). The SDHAF4 constructs were isolated from positive colonies using NucleoSpin Plasmid Mini kit (NoLid) (Macherey-Nagel, 740499) or NucleoBond Xtra Midi kit (Macherey-Nagel, 740410). Final constructs were sequenced by Sanger sequencing (Eurofins Genomics). Throughout construct development, DNA concentration was measured using the NanoDrop ND-2000 device (Thermo Fisher Scientific).

The pCDH-SDHAF4 plasmid was transduced into parental, SDHAF2^{KO}, SDHAF4^{KO36}, and SDHAF2^{KO}/SDHAF4^{KO} hPheo1 cells using recombinant lentiviruses obtained from calcium phosphate-transfected HEK 293 T cells using packaging plasmids psPAX2 (Addgene, 12260) and pMD2.G (Addgene, 12259) and the pCDH-SDHAF4 constructs. The medium containing lentiviral particles was harvested 48 h post-transfection, and the viral particles were precipitated using PEG-it (System Biosciences, LV810A-1). Target cells were transduced with viruses at multiplicity of infection MOI 5–10 and selected for neomycin (200 ug/ml, Sigma A1720) resistance.

SDS-PAGE and Western analyses

Cells were harvested and washed twice with phosphate buffered saline (PBS). For lysis, the cell pellets were resuspended in RIPA (Radio-ImmunoPrecipitation Assay) buffer containing 20 mM Tris (pH 7.5), 150 mM NaCl, 1 mM EDTA, 1 mM EGTA, 1% (v/v) NP-40, 0.1% SDS and 0.5% sodium deoxycholate supplemented with protease inhibitor mix M (Serva) for 30 min with shaking on ice. Lysed cells were centrifuged at 16,000 g for 5 min at 4 °C, and the supernatant was collected for analysis.

For SDS-PAGE, after estimation of protein concentration using the Pierce BCA protein assay kit (Thermo Fisher Scientific, 23225), protein samples (40 μg) were mixed with 4 × Laemmli sample buffer (8% SDS, 260 mM Tris-HCl (pH 6.8), 40% glycerol, 200 mM DTT (Sigma), 0.01% bromophenol blue (Sigma)), boiled for 5 min, and separated on a 12% SDS-PAGE gel.

For western analyses, proteins were transferred from the SDS-PAGE gel onto a 0.45 μm pore nitrocellulose membrane (BioRad, 1620115). The membrane was blocked for 1 h with 5% non-fat milk and incubated with primary antibody in Tris-buffered saline/Tween-20 (TBS-T) supplemented with 2% non-fat milk overnight at 4 °C. The following primary antibodies were used: anti-SDHA (Abcam, ab14715), anti-SDHB (Abcam, ab14714), anti-SDHAF2 (Cell Signaling Technology, 45849), anti-SDHAF4 (Novus, NBP1-86324), and for loading controls anti-Hsp60 (Cell Signaling Technology, 12165), anti-VDAC1 (Abcam, ab15895) or anti-GAPDH (Cell Signaling Technology, 5174). All antibodies were diluted 1:1000 in 2% non-fat milk except for anti-SDHAF4 (1:500 dilution). The membranes were then treated with horseradish peroxidase-conjugated secondary antibodies (goat anti-rabbit, 170-6515, BioRad, or goat anti-mouse, 170-6516, BioRad) diluted 1:10,000 in TBS-T containing 2% non-fat milk for 1 h at room temperature. Blots were imaged (Radiance ECL or Radiance Plus, Azure Biosystems) using AzureSpot 2.0 software (Azure Biosystems).

Isolation of mitochondria and native blue gel electrophoresis

To isolate mitochondria, cells were resuspended in the isolation buffer (250 mM sucrose, 10 mM Tris, 1 mM EDTA) and passed three times through an 8 μm tungsten carbide ball of a Balch homogenizer (Isobiotec) using a hand-driven 1 ml syringe. The homogenate was centrifuged at 800 *g* for 5 min at 4 °C. The supernatant containing mitochondria was collected, and then centrifuged at 3000 g for 5 min to remove additional impurities and at 10,000 g for 15 min to pellet mitochondria. Pelleted mitochondria were washed with the isolation buffer and stored at −80 °C. 10 μg digitonin-solubilized (8 g/g protein) mitochondria were mixed with the sample loading buffer (0.015 μl per 1 μg protein; 0.75 M aminocaproic acid, 50 mM Bis-Tris, 12% glycerol, 0.5 mM EDTA, 5% Coomassie Brilliant Blue G-250) and separated on 4–16% NativePAGE Novex BisTris gradient gels. Electrophoresis ran in three steps, i.e., using the blue cathode buffer (0.02% Coomassie Brilliant Blue G-250) at 35 V for 70 min, and then clear cathode buffer at 25 V overnight. Finally, the voltage was increased to 200 V for 2 h. For western blots, gels were incubated in the transfer buffer for 10 min with 0.1% SDS, and proteins were transferred to 0.2 μm PVDF (polyvinylidene difluoride) 0.2 μm membranes (Biorad). Western analysis after native gel electrophoresis used the same procedure as western analysis following SDS-PAGE (above).

Evaluation of respiration

Respiration was evaluated in digitonin-permeabilized cells as previously described[59–61]. For routine respiration, cells were trypsinized, washed with PBS, resuspended in Mir05 medium (0.5 mM EGTA, 3 mM MgCl2, 60 mM K-lactobionate, 20 mM taurine, 10 mM KH2PO4, 110 mM sucrose, 1 g/l essentially fatty acid-free bovine serum albumin, 20 mM Hepes, pH 7.1 at 30 °C) and transferred to the chamber of Oxygraph-2k instrument (Oroboros). The respiration measurements were performed at 37 °C. After closing the chamber, routine respiration on intracellular substrates was recorded. Access of exogenously added substrates was allowed by permeabilizing the cellular plasma membrane with 5 μg digitonin per million cells. Complex II-mediated respiration was assessed by adding 0.5 μM rotenone, 10 mM succinate, 3 mM ADP and 10 μM cytochrome c together with a CII inhibitor (5 mM malonate). Uncoupled state was achieved by CCCP (carbonyl cyanide m-chlorophenyl hydrazone) titration to obtain the maximal respiratory rate. Antimycin A (2.5 μM) was added at the end of each measurement to inhibit ETC and the residual oxygen consumption after antimycin A addition was subtracted from all results to obtain mitochondria-specific rates.

Immunoprecipitation from cell lysates

hPheo1 cells were transduced with SDHA Myc-DDK-tagged (Origene, RC200349L3) lentiviral particles, which were prepared as stated above. All cell lines were then selected for puromycin (1 mg/ml) resistance. For the immunoprecipitation, 80 μl of protein A/G resin slurry (Thermo, 53132) was washed with RIPA buffer (10 mM Tris pH 7.4, 1 mM EDTA, 150 mM NaCl, 1% Triton X-100) containing EDTA-free protease (Roche, 11873580001) and phosphatase (Thermofisher, A32957) inhibitor cocktail, and incubated with either anti-FLAG IgG, 1:100 dilution (Thermo, PA1-984B; 4 °C/2 h) or IgG control, 1:250 dilution (Cell Signaling, 3900 S) and washed 3 times with RIPA buffer as stated previously. Cell lysates from different hPheo1 sub-lines were obtained using the RIPA lysis buffer containing protease and phosphatase inhibitors. Concentration of proteins was determined using the BCA kit (Thermofisher, 23225), samples were diluted to the same concentration, and 750 μg of protein lysate was loaded on previously prepared A/G beads with bound anti-FLAG IgG (overnight at 4 °C). Samples were washed 3 times with RIPA buffer and eluted with hot (95 °C) SDS-based elution buffer (50 mM Tris pH 6.8, 20% glycerol, 4% SDS, 0.02% BMF, 200 mM DTT). Analysis of samples was performed by western blotting, as described above.

In-gel succinate dehydrogenase (SDH) activity

To measure in-gel SDH activity, 30 μg digitonin-solubilized mitochondria were mixed with 10x sample buffer containing 50% glycerol and 0.1% Ponceau S dye and subjected to high-resolution clear native electrophoresis. Deoxycholate (0.05%) and lauryl maltoside (0.01%) were added to the cathode buffer. Electrophoresis was run on a 4–16% NativePAGE Novex Bis-Tris gel at 35 V for 70 min, then at 25 V overnight followed by 2 h at 200 V. To visualize the activity, gels with separated protein complexes were incubated for 20 min in the assay buffer containing 20 mM sodium succinate, 0.2 mM phenazine methosulfate, and 0.25% nitrotetrazolium blue in 5 mM Tris-HCl (pH 7.4). The reaction was stopped using a solution containing 50% methanol and 10% acetic acid, and gels were immediately photographed.

Evaluation of succinate:quinone reductase activity

Cells grown in 6-well plates were washed with PBS and lysed in 25 mM K_2HPO_4 buffer (pH 7.4) by alternating freezing on dry ice and thawing at 42 °C. Protein lysates (25 μg) were resuspended in 100 mM K_2HPO_4 buffer and transferred to a 96-well plate. The lysates were then incubated in buffer containing 20 mM succinate, 2 μM antimycin A, 5 μM rotenone, 10 mM sodium cyanide, 50 mg/ml bovine serum albumin, and 0.015% w/v 2,6-dichlorophenol indophenol for 5 min. The signal intensity at 600 nm was recorded for 5 min, then 100 μM decylubiquinone was added and the reaction was recorded for another 30 min. Regression analysis of the linear portion of the curve was performed using GraphPad PRISM software (version 8.4.3).

Quantitative real time PCR

Total RNA was obtained using the RNeasy mini kit (Qiagen, 74004). RNA concentration was measured using a NanoDrop 2000 instrument (Thermo Fisher Scientific). First strand cDNA was synthesized from 2 μg of total RNA with random hexamer primers using Revert Aid First strand cDNA Synthesis Kit (Thermo Scientific, K1621). qRT-PCR was performed using the CFX96 Touch Real-Time PCR Detection System (BioRad) with 5xHOT FIREPol Evagreen qPCR Supermix (Solis Biodyne, 08-36-0000 S). The relative quantity of cDNA was estimated by the ΔΔCT method and was normalized to β-actin. The following primers were purchased from Sigma: SDHAF4^{forward}: 5´-GCA AGA TCA CCC CTT CTG TGT-3´, SDHA4F^{reverse} 5´-AAT GGG AAT CCT CTG GTG CAT-3´; β-actin^{forward}: 5´-CCA ACC GCG AGA AGA TGA-3´, β-actin^{reverse} 5´-CCA GAG GCG TAC AGG GAT AG-3´.

Succinate-to-fumarate ratio

Cells were grown in 12-well plates for 24 h, harvested, and washed twice with ice-cold 0.9% NaCl. Metabolites were extracted with 500 μl of 80% methanol in water. After centrifugation for 5 min at 16,000 g at 2 °C, 400 μl of the extract was transferred to a 2-ml glass vial with a screwcap, dried *in vacuo*, and re-dissolved in 100 μl of anhydrous pyridine (Sigma-Aldrich, 270970-100 ML). 30 μl of N-tert-butyldimethylsilyl-N-methyl trifluoroacetamide (Sigma-Aldrich, 394882-5 ML) was added. The content was vortexed and incubated at 70 °C for 30 min under constant shaking, after which 300 μl of hexane (VWR Chemical) was added. The silylated extract was analyzed using two-dimensional gas chromatography with mass spectrometric detection (GC×GC-MS; Pegasus 4D; LECO Corporation). The first dimension was run on an Rxi-5Sil MS column (30 m × 0.25 mm ID × 0.25 μm dF; Restek), and the second dimension was run using a BPX50 column (1–1.5m × 0.1 mm ID × 0.1 μm dF; SGE). Operating conditions were as follows: primary oven temperature gradient of 50 °C (1 min) to 240 °C (10 °C/min steps), and to 320 °C (4 min) (20 °C/min steps); the secondary oven was set at 5 °C above the primary oven temperature; modulation period, 3 to 5 s; injection temperature, 30 °C; split-less injection mode was applied; injection volume, 1 μl; carrier gas, helium; and corrected constant flow, 1 ml/min. MS-detection parameters were as follows: electron ionization, −70 eV; transfer line temperature, 280 °C; and ion source temperature, 280 °C. ChromaTOF software (v.4.51; LECO Corporation) was used to control the instrument, and to acquire and process data.

Succinic and fumaric acids were analyzed as tert-butyl silyl derivatives, with their identities confirmed by co-elution with standards. Analytes were quantified using masses of m/z 289 (succinic acid) and m/z 287 (fumaric acid).

Isotope labeling of SDHAF4 for NMR

Isotope labeling of His_6-SDHAF4 with ^{15}N and ^{13}C for NMR experiments was done by growing *E. coli* BL21(*DE3*) in M9 minimal media supplemented with ^{13}C glucose and ^{15}N ammonium chloride (Cambridge Isotopes). Protein was purified using Ni^{2+} affinity chromatography followed by size exclusion chromatography on a 24 ml Superdex S200 increase column (Superdex S200 increase, Cytiva, 28990944) in 20 mM HEPES pH 7.5, 1 mM TCEP. Purified protein was exchanged in 20 mM sodium phosphate pH 6.5, 3 mM TCEP buffer using a second step of size exclusion chromatography on a Superdex S200 increase column. Protein was concentrated to 10 mg/ml using a 3 kDa Amicon filtration unit.

NMR spectroscopy

NMR experiments were performed at 298 K on a Bruker AV-III 600.13 and 900.13 MHz spectrometer equipped with triple resonance cryogenically cooled CPTCI probes. All experiments were recorded with 9.5 mg/ml His_6-SDHAF4 in 550 μl H_2O/D_2O 95:5 (~1 mM), containing

20 mM sodium phosphate, 10 mM Tris (2-carboxylethyl) phosphine (TCEP), and ~0.5 mM of 4,4-dimethyl-4-silapentane-1-sulfonic acid (DSS) for reference. NMR spectra were processed using Topspin 3.6 (Bruker BioSpin) and analyzed with NMRViewJ (One Moon Scientific, Inc.). Standard ^{1}H-^{15}N HSQC experiments were used. Backbone resonance assignment required two steps. The first step measured and analyzed three sets of carbon direct detect measurements. The second step used the traditional amide-based method. The carbon direct detect experiments were the CON, hcaCOncaNCO, and hcacoNcaNCO[62]. The amide-based experiments were standard HNCO, HNcaCO, HNCA, HNcoCA, CBCAcoNH, HNCACB, and HSQC experiments[63]. Data acquisition parameters are described in Supplementary Table 3.

NMR data analysis

Obstacles in assigning the SDHAF4 peptide included: (1) the limited signal dispersion in the absence of secondary structure; (2) the high percentage of prolines (about 10% of all residues), which broke the connectivities in the traditional assignment scheme because they lack amide protons; and (3) an apparent presence of a major and a minor form, as seen in the ^{15}N HSQC spectrum that could not be readily separated (Supplementary Fig. 5e). Therefore, an alternative assignment method was used, where all C' and N backbone atoms were initially assigned using the carbon direct detect experiments with the highest sensitivity and resolution measured at 900 MHz and a cold carbon channel[64]. This information served as a bases for the traditional amide-based assignment. using a data set of the following 3D spectra: HNCO, HNcaCO, HNCA, HNcoCA, CBCAcoNH, HNCACB spectra[63]. The use of these two assignment strategies provided the necessary spectral resolution and continuous connectivity, allowing for 99% assignment of all N, C', ^{1}HN, ^{13}C$_\alpha$, ^{13}C$_\beta$ atoms following the 6xHis N-terminal tag, starting at SDHAF^{E20}. Assignment of the N and C' atoms from SDHAF^{H16} to the terminal SDHAF^{F108} were complete. HN, C$_\alpha$, C$_\beta$, were fully assigned immediately following the 6xHis N-terminal tag, with the exception for SDHAF4^{S35} (HN, C$_\alpha$, C$_\beta$) and SDHAF4S^{S36}(HN), which could not be assigned because no unambiguous peaks were found for them. Several amide peaks in the HSQC spectrum are weak with SDHAF4^{S34} only being visualized when lowering the contour level almost to the noise level. All other missing assignments were expected, such as the C$_\beta$ atoms of the glycine residue, and the missing amide protons for the prolines. Given challenges in assigning spectra of intrinsically disordered proteins, the chemical shift index (CSI) analysis was performed using four programs in parallel. The first program, Talos+ (Supplementary Fig. 5h), uses the order parameter S^2 which shows high flexibility for most residues pointing to a low probability of secondary structure[65]. To validate these results, we repeated the analysis using chemical shift secondary structure population inference (CheSPI; Supplementary Fig. 5i)[66], Poulsen[67], and POTENCI[68]. All analyses are consistent with SDHAF4 as an intrinsically disordered protein. The assigned HSQC and CON spectra are shown in Supplementary Fig. 5e, f.

Crystallization, data collection, and structure determination

The SDHA-AF2-AF4 complex was prepared by incubating purified holo-SDHA-SDHAF2 complex with purified His$_6$-SDHAF4 for 5 h at 4 °C at a protein concentration of 0.5 mg/ml in 20 mM HEPES pH 7.5, 1 mM DTT. The protein solution was then concentrated and subjected to size exclusion chromatography on a Superdex S200 increase column (Superdex S200 increase, Cytiva, 28990944) in the same buffer. The SDHA-AF4 complex was prepared by incubating purified holo-SDHA-AF2 with His$_6$-SDHAF4 at 25 °C overnight followed by size exclusion chromatography on a Superdex S200 increase column (GE Healthcare) in the same buffer.

The SDHA-AF2-AF4 complex was crystallized using the hanging drop vapor diffusion method mixing the complex (12 mg/ml) with reservoir solution (0.2 M ammonium citrate tribasic pH 8.0, 20% w/v polyethylene glycol 3,350 and 1 mM DTT) at 1:1 ratio at 25 °C. The SDHA-SDHAF4 complex was crystallized by mixing proteins (14 mg/ml) at 1:1 ratio with reservoir solution containing 100 mM sodium malonate pH 4.7, 12% PEG 3350, and 1 mM DTT. For cryoprotection, the crystals of both complexes were dipped into a solution containing all components of the reservoir and a final concentration of 20% ethylene glycol prior to flash cooling in liquid nitrogen.

Diffraction data were collected at LS-CAT beamline ID-F (λ = 0.97872) equipped with MARMOSAIC 225 CCD detector. Data were collected at a temperature of 100 K for both SDHA-AF2-AF4 and SDHA-AF4 crystals. The data were indexed, integrated, and scaled using HKL2000[69]. Unit cell parameters and data collection statistics are listed in Supplementary Table 1.

Structure determination and refinement

The structure of SDHA-AF2-AF4 was determined by molecular replacement using the Phaser subroutine[70] in Phenix[71] with the SDHA-AF2 complex (PDB entry 3VAX[32]) as the search model. SDHAF4 was modeled manually into the $|F_o| - |F_c|$ difference electron density in COOT[72]. The structure of SDHA-AF4 was determined by molecular replacement following the removal of SDHAF2 from the resultant SDHA-AF2-AF4 structure. Structures were refined by standard methods by alternating model building in COOT[72] and refinement in Phenix[71].

Statistics and reproducibility

The statistical methods used in the data analysis are indicated in the corresponding figure legends and were selected depending on the groups being compared. This study contains cell line experiments validated by the independent creation of duplicate cell lines. Because the exact numbers of cells could not be determined, we instead normalized the assay by using loading controls. Data was excluded for these experiments when the loading control was not consistent for all groups. No statistical method was used to predetermine sample size. The experiments were not randomized, and blinding was not performed.

Structural work used standards in the field to exclude diffraction spots that were statistical outliers, as assessed by HKL2000[71]. Diffraction spots were also excluded if they were beyond the resolution cutoff, as determined by a composite evaluation of R_{sym}, completeness, I/σ, and $CC_{1/2}$.

Reporting summary

Further information on research design is available in the Nature Portfolio Reporting Summary linked to this article.

Data availability

PDB coordinates and processed diffraction data generated in this study have been deposited in the Protein Data Bank (https://wwpdb.org/) with accession codes 8DYD and 8DYE. Raw diffraction data have been deposited with SBGrid (http://data.sbgrid.org) with accession codes and direct hyperlinks of 954 and 955. NMR Chemical shift data for SDHAF4 have been deposited in the BMRB databank (http://www.bmrb.wisc.edu), retrievable under the accession number 52207. Source data are provided with this paper. Other PDB entries used in this study and their description: The human SDHA-AF2 complex, PDB entry 3VAX[32] was used for molecular replacement. Porcine mitochondrial Complex II, PDB entry 3SFD[73] was used for showing assembled complex II in Fig. 7. The following PDBs are cited in the discussion: 4F7U[42], 1ZYI[43], 1U96[44], 1U97[44], 2GT5[45], 2GQK[45], 2GQM[45], 3P2D[46], 5TV1[47], 7SQU[52], 5XTD[53], 2JYA[54], 2JRR[55]. Source data are provided with this paper.

References

1. Ryan, D. G. et al. Coupling Krebs cycle metabolites to signalling in immunity and cancer. *Nat. Metab.* 1, 16–33 (2019).

2. Murphy, M. P.& O'Neill, L. A. J. Krebs cycle reimagined: the emerging roles of succinate and itaconate as signal transducers. *Cell* 174, 780–784 (2018).
3. Murphy, M. P. & Chouchani, E. T. Why succinate? Physiological regulation by a mitochondrial coenzyme Q sentinel. *Nat. Chem. Biol.* 18, 461–469 (2022).
4. Iverson, T. M., Maklashina, E. & Cecchini, G. Structural basis for malfunction in complex II. *J. Biol. Chem.* 287, 35430–35438 (2012).
5. Iverson, T. M., Singh, P. K. & Cecchini, G. An evolving view of complex II-noncanonical complexes, megacomplexes, respiration, signaling, and beyond. *J. Biol. Chem.* 299, 104761 (2023).
6. Gottlieb, E. & Tomlinson, I. P. Mitochondrial tumour suppressors: a genetic and biochemical update. *Nat. Rev. Cancer* 5, 857–866 (2005).
7. Gupta, P. et al. Genetic impairment of succinate metabolism disrupts bioenergetic sensing in adrenal neuroendocrine cancer. *Cell Rep.* 40, 111218 (2022).
8. Vinogradov, A. D., Winter, D. & King, T. E. The binding site for oxaloacetate on succinate dehydrogenase. *Biochem. Biophys. Res. Commun.* 49, 441–444 (1972).
9. Priegnitz, A., Brzhevs.kaya, O. N. & Wojtczak, L. Tight binding of oxaloacetate to succinate dehydrogenase. *Biochem. Biophys. Res. Commun.* 51, 1034–1041 (1973).
10. Gutman, M. & Silman, N. The steady state activity of succinate dehydrogenase in the presence of opposing effectors.II. Reductive activation of succinate dehydrogenase in presence of oxaloacetate. *Mol. Cell Biochem.* 7, 177–185 (1975).
11. Huang, L. S. et al. 3-nitropropionic acid is a suicide inhibitor of mitochondrial respiration that, upon oxidation by complex II, forms a covalent adduct with a catalytic base arginine in the active site of the enzyme. *J. Biol. Chem.* 281, 5965–5972 (2006).
12. Beal, M. F. et al. Neurochemical and histologic characterization of striatal excitotoxic lesions produced by the mitochondrial toxin 3-nitropropionic acid. *J. Neurosci.* 13, 4181–4192 (1993).
13. Renkema, G. H. et al. SDHA mutations causing a multisystem mitochondrial disease: novel mutations and genetic overlap with hereditary tumors. *Eur. J. Hum. Genet.* 23, 202–209 (2015).
14. Birch-Machin, M. A., Taylor, R. W., Cochran, B., Ackrell, B. A. & Turnbull, D. M. Late-onset optic atrophy, ataxia, and myopathy associated with a mutation of a complex II gene. *Ann. Neurol.* 48, 330–335 (2000).
15. Burnichon, N. et al. SDHA is a tumor suppressor gene causing paraganglioma. *Hum. Mol. Genet.* 19, 3011–3020 (2010).
16. Sharma, P., Maklashina, E., Cecchini, G. & Iverson, T. M. Maturation of the respiratory complex II flavoprotein. *Curr. Opin. Struct. Biol.* 59, 38–46 (2019).
17. Moosavi, B., Berry, E. A., Zhu, X. L., Yang, W. C. & Yang, G. F. The assembly of succinate dehydrogenase: a key enzyme in bioenergetics. *Cell Mol. Life Sci.* 76, 4023–4042 (2019).
18. Van Vranken, J. G., Na, U., Winge, D. R.& Rutter, J. Protein-mediated assembly of succinate dehydrogenase and its cofactors. *Crit. Rev. Biochem. Mol. Biol.* 50, 168–180 (2015).
19. Cecchini, G. Function and structure of complex II of the respiratory chain. *Annu. Rev. Biochem.* 72, 77–109 (2003).
20. Bezawork-Geleta, A. et al. Alternative assembly of respiratory complex II connects energy stress to metabolic checkpoints. *Nat. Commun.* 9, 2221 (2018).
21. Reynolds, M. B. et al. Cardiolipin coordinates inflammatory metabolic reprogramming through regulation of Complex II disassembly and degradation. *Sci. Adv.* 9, eade8701 (2023).
22. Chouchani, E. T. et al. Ischaemic accumulation of succinate controls reperfusion injury through mitochondrial ROS. *Nature* 515, 431–435 (2014).
23. Lemarie, A., Huc, L., Pazarentzos, E., Mahul-Mellier, A. L. & Grimm, S. Specific disintegration of complex II succinate:ubiquinone oxidoreductase links pH changes to oxidative stress for apoptosis induction. *Cell Death Differ.* 18, 338–349 (2011).
24. Pfleger, J., He, M. & Abdellatif, M. Mitochondrial complex II is a source of the reserve respiratory capacity that is regulated by metabolic sensors and promotes cell survival. *Cell Death Dis.* 6, e1835 (2015).
25. Ghezzi, D. et al. SDHAF1, encoding a LYR complex-II specific assembly factor, is mutated in SDH-defective infantile leukoencephalopathy. *Nat. Genet.* 41, 654–656 (2009).
26. Hao, H. X. et al. SDH5,a gene required for flavination of succinate dehydrogenase, is mutated in paraganglioma. *Science* 325, 1139–1142 (2009).
27. Na, U. et al. The LYR factors SDHAF1 and SDHAF3 mediate maturation of the iron-sulfur subunit of succinate dehydrogenase. *Cell Metab.* 20, 253–266 (2014).
28. Van Vranken, J. G. et al. SDHAF4 promotes mitochondrial succinate dehydrogenase activity and prevents neurodegeneration. *Cell Metab.* 20, 241–252 (2014).
29. Bezawork-Geleta, A., Rohlena, J., Dong, L., Pacak, K. & Neuzil, J. Mitochondrial complex II: at the crossroads. *Trends Biochem. Sci.* 42, 312–325 (2017).
30. Wang, X. et al. Hepatic suppression of mitochondrial complex II assembly drives systemic metabolic benefits. *Adv. Sci. (Weinh)* 9, e2105587 (2022).
31. Kudryavtseva, A. V. et al. Mutation profiling in eight cases of vagal paragangliomas. *BMC Med. Genomics* 13, 115 (2020).
32. Sharma, P., Maklashina, E., Cecchini, G. & Iverson, T. M. The roles of SDHAF2 and dicarboxylate in covalent flavinylation of SDHA, the human complex II flavoprotein. *Proc. Natl. Acad. Sci. USA* 117, 23548–23556 (2020).
33. Maklashina, E., Iverson, T. M. & Cecchini, G. How an assembly factor enhances covalent FAD attachment to the flavoprotein subunit of complex II. *J. Biol. Chem.* 298, 102472 (2022).
34. Belt, K., Van Aken, O., Murcha, M., Millar, A. H.& Huang, S. An assembly factor promotes assembly of flavinated SDH1 into the succinate dehydrogenase complex. *Plant Physiol.* 177, 1439–1452 (2018).
35. Wang, X. et al. Cardiac disruption of SDHAF4-mediated mitochondrial complex II assembly promotes dilated cardiomyopathy. *Nat. Commun.* 13, 3947 (2022).
36. Ghayee, H. K. et al. Progenitor cell line (hPheo1) derived from a human pheochromocytoma tumor. *PLoS One* 8, e65624 (2013).
37. Maklashina, E., Rajagukguk, S., Iverson, T. M. & Cecchini, G. The unassembled flavoprotein subunits of human and bacterial complex II have impaired catalytic activity and generate only minor amounts of ROS. *J. Biol. Chem.* 293, 7754–7765 (2018).
38. Eletsky, A. et al. Solution NMR structure of yeast succinate dehydrogenase flavinylation factor Sdh5 reveals a putative Sdh1 binding site. *Biochemistry* 51, 8475–8477 (2012).
39. Cecchini, G. Respiratory complex II: role in cellular physiology and disease. *Biochim. Biophys. Acta* 1827, 541–542 (2013).
40. Spinelli, J. B. et al. Fumarate is a terminal electron acceptor in the mammalian electron transport chain. *Science* 374, 1227–1237 (2021).
41. Kumar, R. et al. A redox cycle with complex II prioritizes sulfide quinone oxidoreductase-dependent H2S oxidation. *J. Biol. Chem.* 298, 101435 (2022).
42. Grimm, C. et al. Structural basis of assembly chaperone- mediated snRNP formation. *Mol. Cell* 49, 692–703 (2013).
43. Furst, J. et al. ICln159 folds into a pleckstrin homology domain-like structure. Interaction with kinases and the splicing factor LSm4. *J. Biol. Chem.* 280, 31276–31282 (2005).
44. Abajian, C., Yatsunyk, L. A., Ramirez, B. E. & Rosenzweig, A. C. Yeast cox17 solution structure and Copper(I) binding. *J. Biol. Chem.* 279, 53584–53592 (2004).

45. Banci, L. et al. A hint for the function of human Sco1 from different structures. *Proc. Natl Acad. Sci. USA* 103, 8595–8600 (2006).
46. Zhan, X., Gimenez, L. E., Gurevich, V. V.& Spiller, B. W. Crystal structure of arrestin-3 reveals the basis of the difference in receptor binding between two non-visual subtypes. *J. Mol. Biol.* 406, 467–478 (2011).
47. Chen, Q. et al. Structural basis of arrestin-3 activation and signaling. *Nat. Commun.* 8, 1427 (2017).
48. Huang, W. et al. Structure of the neurotensin receptor 1 in complex with beta-arrestin 1. *Nature* 579, 303–308 (2020).
49. Staus, D. P. et al. Structure of the M2 muscarinic receptor-beta-arrestin complex in a lipid nanodisc. *Nature* 579, 297–302 (2020).
50. Chaikeeratisak, V. et al. Assembly of a nucleus-like structure during viral replication in bacteria. *Science* 355, 194–197 (2017).
51. Mendoza, S. D. et al. A bacteriophage nucleus-like compartment shields DNA from CRISPR nucleases. *Nature* 577, 244–248 (2020).
52. Laughlin, T. G. et al. Architecture and self-assembly of the jumbo bacteriophage nuclear shell. *Nature* 608, 429–435 (2022).
53. Guo, R., Zong, S., Wu, M., Gu, J. & Yang, M. Architecture of human mitochondrial respiratory megacomplex I(2)III(2)IV(2). *Cell* 170, 1247–1257.e1212 (2017).
54. Lemak, A. et al. NMR solution structure of protein ATU1810 from Agrobacterium tumefaciens. Northeast Structural Genomics Consortium target AtR23, Ontario Centre for Structural Proteomics Target ATC1776. *Northeast Structural Genomics Consortium (NESG), Ontario Centre for Structural Proteomics (OCSP)*, https://doi.org/10.2210/pdb2JYA/pdb (2007).
55. Swapna, G. V. T. et al. Solution NMR Structure of Q5LLS5 from Silicibacter Pomeroy. Northeast Structural Genomics Consortium target SiR90. *Northeast Structural Genomics Consortium (NESG)*, https://doi.org/10.2210/pdb2JRR/pdb (207).
56. Baradaran, R., Berrisford, J. M., Minhas, G. S. & Sazanov, L. A. Crystal structure of the entire respiratory complex I. *Nature* 494, 443–448 (2013).
57. Tan, S., Kern, R. C.& Selleck, W. The pST44 polycistronic expression system for producing protein complexes in Escherichia coli. *Protein Expr. Purif.* 40, 385–395 (2005).
58. Zetsche, B. et al. Multiplex gene editing by CRISPR-Cpf1 using a single crRNA array. *Nat. Biotechnol.* 35, 31–34 (2017).
59. Bajzikova, M. et al. Reactivation of dihydroorotate dehydrogenase-driven pyrimidine biosynthesis restores tumor growth of respiration-deficient cancer cells. *Cell Metab.* 29, 399–416.e310 (2019).
60. Rohlenova, K. et al. Selective disruption of respiratory super-complexes as a new strategy to suppress Her2(high) breast cancer. *Antioxid. Redox. Signal.* 26, 84–103 (2017).
61. Boukalova, S. et al. Mitochondrial targeting of metformin enhances its activity against pancreatic cancer. *Mol. Cancer Ther.* 15, 2875–2886 (2016).
62. Pantoja-Uceda, D. & Santoro, J. Direct correlation of consecutive C'-N groups in proteins: a method for the assignment of intrinsically disordered proteins. *J. Biomol. NMR* 57, 57–63 (2013).
63. Sattler, M., Schleucher, J. & Griesinger, C. Heteronuclear multi-dimensional NMR experiments for the structure determination of proteins in solution employing pulsed field gradients. *Prog. Nucl. Mag. Res. Spectrosc* 34, 93–158 (1999).
64. Voehler, M., Ashoka, M. A., Meiler, J. & Bock, P. E. Carbon and amide detect backbone assignment methods of a novel repeat protein from the staphylocoagulase in S-aureus. *Biomol. Nmr Assign.* 11, 243–249 (2017).
65. Borcherds, W. M.& Daughdrill, G. W. Using NMR chemical shifts to determine residue-specific secondary structure populations for intrinsically disordered proteins. *Methods Enzymol.* 611, 101–136 (2018).
66. Nielsen, J. T. & Mulder, F. A. A. CheSPI: chemical shift secondary structure population inference. *J. Biomol. NMR* 75, 273–291 (2021).
67. Kjaergaard, M. & Poulsen, F. M. Sequence correction of random coil chemical shifts: correlation between neighbor correction factors and changes in the Ramachandran distribution. *J. Biomol. NMR* 50, 157–165 (2011).
68. Nielsen, J. T. & Mulder, F. A. A. POTENCI: prediction of temperature, neighbor and pH-corrected chemical shifts for intrinsically disordered proteins. *J. Biomol. NMR* 70, 141–165 (2018).
69. Otwinowski, Z. & Minor, W. Processing of X-ray diffraction data collected in oscillation mode. *Methods Enzymol.* 276,307–326 (1997).
70. McCoy, A. J. et al. Phaser crystallographic software. *J. Appl. Crystallogr.* 40, 658–674 (2007).
71. Adams, P. D. et al. PHENIX: a comprehensive Python-based system for macromolecular structure solution. *Acta Crystallogr. D Biol. Crystallogr.* 66, 213–221 (2010).
72. Emsley, P. & Cowtan, K. Coot: model-building tools for molecular graphics. *Acta Crystallogr. D Biol. Crystallogr.* 60, 2126–2132 (2004).
73. Zhou, Q. et al. Thiabendazole inhibits ubiquinone reduction activity of mitochondrial respiratory complex II via a water molecule mediated binding feature. *Protein Cell* 2, 531–542 (2011).
74. Taylor, R. W. et al. Deficiency of complex II of the mitochondrial respiratory chain in late-onset optic atrophy and ataxia. *Ann. Neurol.* 39, 224–232 (1996).
75. Blaut, M. et al. Fumarate reductase mutants of Escherichia coli that lack covalently bound flavin. *J. Biol. Chem.* 264, 13599–13604 (1989).
76. Sun, F. et al. Crystal structure of mitochondrial respiratory membrane protein complex II. *Cell* 121, 1043–1057 (2005).

Acknowledgements

We thank EA Berry, J Hirboo, and V Segal for their comments on the manuscript during preparation. We thank F Mulder for assistance with NMR analysis using CheSPI. This research used resources of the Advanced Photon Source, a U.S. Department of Energy (DOE) Office of Science User Facility operated for the DOE Office of Science by Argonne National Laboratory under Contract No. DE-AC02-06CH11357. Use of the LS-CAT Sector 21 was supported by the Michigan Economic Development Corporation and the Michigan Technology Tri-Corridor (Grant 085P1000817). Use of the Advanced Photon Source was supported by the United States Department of Energy, Office of Basic Energy Sciences, under contract DE-AC02-06CH11357. NMR data were collected at the Vanderbilt Center for Structural Biology NMR core facility, which is supported in part by the National Science Foundation award 0922862, U.S. National Institutes of Health award S10 RR025677 and R35GM118089-04S1, and Vanderbilt University matching funds. This work was supported by National Institutes of Health award GM61606 (GC/TMI). GC is the recipient of a Senior Research Career Scientist award IK6BX004215 from the Department of Veterans Affairs. P.S. was supported by Postdoctoral Fellowship 19POST34450093 from the American Heart Association. This work was also supported in part by the Czech Science foundation awards to J.N. (20-05942 S and 21-04607X), J.R. (19-20553 S), S.B. (20-11724Y and 23-05303 S) and T.M. (20-25768 S). and a Czech Health Foundation award to S.D. (NU23-03-00226). Infrastructure support was provided by Czech Academy of Sciences for the Institute of Biotechnology (RVO86652036).

Author contributions

Conceptualization: T.M.I., G.C., J.N., J.R., E.M., and P.S.; methodology: P.S., E.M., M.V., S.D., S. Balintova, M.K., K.H.V., S. Boukalova, H.G., R.Z., Z.N., J.R., K.C., T.M.; Funding acquisition: J.N., J.R., T.M.I., and G.C. Writing-original draft: P.S., T.M.I., E.M., G.C., and J.N. Writing-review & editing: T.M.I., G.C., J.N., J.R., P.S., E.M., M.V., S.D., S. Balintova, and K.P.

Competing interests

The authors declare no competing interests.

Additional information

Supplementary information The online version contains supplementary material available at https://doi.org/10.1038/s41467-023-44563-7.

Correspondence and requests for materials should be addressed to Jiri Neuzil, Gary Cecchini or T. M. Iverson.

Peer review information *Nature Communications* thanks the anonymous reviewers for their contribution to the peer review of this work. A peer review file is available.

Reprints and permissions information is available at http://www.nature.com/reprints